Journal of
Instrumentation

TECHNICAL REPORT • OPEN ACCESS

Spectroscopic camera system at Wendelstein 7-X

To cite this article: T. Kremeyer *et al* 2025 *JINST* **20** T04003

Published by IOP Publishing for Sissa Medialab

Received: *February 10, 2025*
Revised: *February 24, 2025*
Accepted: *March 4, 2025*
Published: *April 8, 2025*

TECHNICAL REPORT

Spectroscopic camera system at Wendelstein 7-X

T. Kremeyer[a,*] **M. Krause**,[a] **S. Fischer**,[a] **P. Drewelow**[a] **C. Biedermann**[a] **V. Winters**[a] **Y. Gao**[a] **D. Gradic**[a] **M.W. Jakubowski**[a,b] **S. Mohr**,[a] **F. Pisano**[c] **and W7-X Team**[a,1]

[a] *Max-Planck-Institut für Plasmaphysik, Greifswald, Germany*
[b] *University of Szczecin, Institute of Physics, Szczecin, Poland*
[c] *University of Cagliari, Cagliari, Italy*

E-mail: thierry.kremeyer@ipp.mpg.de

Abstract: A network of spectroscopic cameras was installed and successfully operated during the entire operation phase 1 of the optimized stellarator, Wendelstein 7-X. This diagnostic system enabled spatially resolved measurements of photon fluxes at specific wavelengths. Narrow band pass filters in the optical path allowed for targeted photon flux measurements of various spectral lines, specifically for the main ion species, hydrogen, and the primary impurity, carbon.

The cameras were arranged in a stellarator-symmetric configuration, with one camera assembly per half-module. Each camera was equipped with a 135 ° ultra-wide field-of-view lens centered on the divertor, enabling comprehensive observation of the entire divertor unit, including the baffle and most of the surrounding heat shield. This configuration achieved coverage of 56 % of all plasma-facing surfaces at W7-X, providing a spatial resolution up to 1.4 pixel/cm at a frame rate of 25 Hz.

This diagnostic system supports a wide range of applications, from studies of ionizing particle fluxes and wall recycling to investigations of plasma radiation and detachment, edge impurity sources, and their distribution. This paper details the diagnostic system's observation geometry, measurement principles, calibration processes, inter-diagnostic comparisons, synthetic diagnostic modeling, and plans for further development.

Keywords: Plasma diagnostics - charged-particle spectroscopy; Plasma diagnostics - interferometry, spectroscopy and imaging; Detector cooling and thermo-stabilization; Photon detectors for UV, visible and IR photons (solid-state)

*Corresponding author.

[1] For the full list of the W7-X Team members, see the author list of Olaf Grulke et al. *Nucl. Fusion* **64** (2024) 112002 [1].

https://doi.org/10.1088/1748-0221/20/04/T04003

Contents

2025 JINST 20 T04003

1 Introduction

Wendelstein 7-X (W7-X) is a superconducting, modular stellarator designed to explore neo-classical optimized confinement combined with an island divertor in a steady-state plasma, pushing forward the concept of stellarators as viable fusion power plants [2]. The plasma-facing components (PFCs) within the device are tailored to follow the unique three-dimensional structure of the plasma. Comprehensive diagnostic tools are essential for accurately monitoring and analyzing plasma behavior and its interactions with PFCs. In this context, spectroscopic diagnostics play a critical role in assessing particle fluxes, impurity distributions, and plasma-surface interactions, which provide insights into

plasma behavior under varying conditions. This paper presents a novel spectroscopic observation system developed for W7-X, detailing its purpose and operational principles in section 2. The sections that follow are organized as described: section 3 discusses the hardware architecture, starting closest to the plasma with the immersion tube vacuum barrier (sub-section 3.1), the optical path (sub-section 3.2), and the data acquisition (DAQ) system in sub-section 3.3. Section 4 describes the calibration processes including a inter-diagnostic comparison, and section 5 presents synthetic diagnostic modeling. Operational challenges are discussed in section 6. Section 7 concludes with a summary and outlook.

2 Diagnostics purpose and principle

Wendelstein 7-X (W7-X) requires PFCs and a plasma vessel that follow the 3D contour of the plasma itself, limiting assumptions based on axial symmetry. This necessitates a full, spatially resolved observation of primary PFCs. Operation began with a limiter configuration in operation phase 1.1 (OP1.1), followed by the installation of ten inertially cooled island divertor units (TDUs) made of fine grained graphite and a graphite heat shield in OP1.2 [3–5]. For OP2, the TDU was replaced by a water-cooled high-heat-flux (HHF) divertor made of carbon-fiber composite with the same target geometry. The device's five-fold symmetry was preserved for the divertor concept with target plates at ten stellarator symmetric positions, with one upper and one lower divertor per module in a resonant island divertor configuration.

Molecules, atoms and ions of the main plasma species as well as impurities emit radiation when transitions of electrons occur between the various energy levels of the atomic system. At W7-X the knowledge of these transitions allows the analysis of particle fluxes [6], plasma-surface interaction [7], edge temperature and density measurements [8, 9], charge exchange recombination [10], impurity temperatures [11] as well as sources [12] and several other properties [13, 14]. The basis for these studies is the accurate measurement of the photon emission for the specific spectral line of interest.

At W7-X, multiple spectral diagnostics measure the line radiation emitted by various neutral and partially ionized plasma species [15]. Most of them collect light from a single line-of-sight (LOS) and analyze it spectroscopically [16]. The photon flux $\Phi_{H\alpha}$ can be interpreted as the total flux of neutrals ionizing in the plasma by the use of effective S/XB coefficients [6]. The ionizing behaviour of the recycling neutral particles depends on the plasma conditions (T_e, n_e) at the location of re-ionization which can vary significantly between the divertor, baffle, heat shield, and steel panel regions. Recycling particles can also undergo significant neutral transport between neutralisation and re-ionization [6, 17]. Accordingly, it is necessary to measure the spectral emissions over a large area, ideally from all PFCs. The spectroscopic observation system presented in this paper can fulfill this requirement. Each camera system detects a specific line radiation from a wide field of view (FOV) with a spatial resolution of between 1.2 pixel/cm and 1.4 pixel/cm depending on the far or close end of the observed horizontal divertor target. The 2D camera frame rate of 25 Hz is lower, compared to single LOS spectral diagnostics that can reach up to 100 kHz[16]. For all photon flux measurements, the measurement is line integrated along the LOS, however synthetic diagnostics can provide information about the emission profile along the LOS as presented in section 5 [18].

2025 JINST 20 T04003

3 Diagnostic hardware

Diagnostics at W7-X must operate under the demanding interplay of high magnetic fields, ultra-high vacuum (UHV) conditions, intense thermal loads, and stringent mechanical constraints. The thermal loads acting on diagnostics include plasma radiation, electron cyclotron resonance heating (ECRH) stray radiation, fast particle losses from the neutral beam injection (NBI), and heat generated by the diagnostic system itself.

Each diagnostic must operate in the present magnetic field and adhere to stringent W7-X vacuum requirements, including restrictions on allowed materials, specific design guidelines, approved welding procedures, rigorous cleaning protocols, compatibility with bake-out temperatures up to 150 °C, and minimized outgassing, particularly of hydrocarbons.

Plasma radiation impinges on the specific camera diagnostic ports with intensities of up to $62\,\mathrm{kW/m^2}$, primarily in the ultraviolet and soft X-ray spectral regions. This radiation is mostly absorbed by the plasma-facing components of the diagnostics.

A fraction of the ECRH power not absorbed by the plasma can enter the immersion tube through vacuum windows [19]. Stray radiation fluxes can reach up to $110\,\mathrm{kW/m^2}$, with absorption rates of approximately 10 % on graphite surfaces and 1 % on stainless steel surfaces.

Neutral beam injection can result in the loss of accelerated particles at the plasma edge. If these particles ionize and become trapped between magnetic wells, their drift motion can lead to deposition on the plasma vessel or diagnostic ports. Simulations have predicted such particle losses for the spectroscopic camera ports, prompting the implementation of countermeasures [20, 21].

Optical diagnostics must be designed to withstand in-vessel conditioning procedures, such as boronization [22], and protect optical components from unintended surface coatings.

Two technical solutions are employed at W7-X to meet these demanding magnetic, thermal, and mechanical requirements: the immersion tube and the endoscope systems [23, 24]. This paper focuses on the immersion tube system, which ensures compliance with all constraints while enabling high-quality spectroscopic measurements. Originally designed for Heating Energy Stage 1 (HE1), the system was upgraded to meet the requirements of Heating Energy Stage 2 (HE2) during OP2. Looking ahead to OP2.4, Heating Energy Stage 3 (HE3) will necessitate significant enhancements in operational capabilities, as summarized in table 1. To meet these extended demands, the immersion tubes will be fully replaced by the endoscope system.

The diagnostic access points in W7-X are limited to port tubes situated between magnetic field coils, exposing components to magnetic field strengths of up to 2.4 T. These ports are labeled with three letters and two digits.

- Lettering: indicates the type and location of the port, present in multiple modules.
- Digits: define the toroidal location — 1 to 5 for the module and 0 or 1 for the half-module.

During operation phase OP1.1, immersion tubes were installed in all AEF ports, each equipped with two spectroscopic cameras (designated A and B) and an infrared (IR) camera. 20 visible camera systems were installed at W7-X, with A and B sharing FOV cones to enable simultaneous observation through two different line radiation filters.

- AEFX0 cameras: observe the lower divertor units.

2025 JINST 20 T04003

Table 1. Pulse cycles for thermomechanical layout (minimum requirements).

Heating energy stages	**HE1**	**HE2**	**HE3**	**HE4**	**HE5**
Maximum power per pulse [MW]		10			24
Plasma pulse duration [s]		10			10
Energy per pulse [MJ]		100			240
Pulses per day / Dwell time		30 / 900			30 / 900
Plasma pulse duration [s]	100	200	600	1800	
Energy [GJ] per pulse	1	2	6	18	
Pulses per day			1		
Imparted energy per day [GJ]	**4**	**5**	**9**	**21**	**7.2**

Note: a definition of the imparted energy requirements in accordance with the staged approach is proposed in terms of heating energy (HE) stages as an independent way of specifying the design targets until OP2.4. The pulse cycles summarized are a specification for design calculations and not an operating instruction.

- AEFX1 cameras: observe the upper divertor units.

The FOV from the AEF ports encompasses all 10 divertor regions, as illustrated in figure 1. The FOV fully covers the horizontal and vertical divertor target, the surrounding baffle, as well as fractions of the heat shield and steel panels as illustrated in figure 2. However, the hardening modifications to the immersion tube (subsection 3.1) resulted in a reduction of the FOV, with the diminished area highlighted in orange. As a result, the high iota section of the horizontal target is no longer observable. Particle flux analysis of magnetic configurations that are intercepted by this section of the target, i.e. the high iota configuration are thus no longer feasible. Analysis of other configurations with loads in the low-iota section are still feasible, however a comparison with data with the full FOV from previous operational phases should be conducted to quantify the fraction of unobserved photon emission in the small section in the low-iota region that is now outside the FOV. A camera image with the full calibration applied as described in 4 is depicted in figure 3. The H_α photon flux is laid over the CAD model of different PFCs through the applied spatial calibration in the scene model.

Key adjustments to the diagnostic hardware were implemented in subsequent operational phases. During OP1.2, several important modifications were made: the immersion tube in AEF50 was replaced by a prototype endoscope [25], AEF30B was configured with an image guide for coherence imaging spectroscopy (QRI) [26], and AEF51B was fitted with a fiber-optic bundle for a high-resolution spectrometer diagnostic (QSS) [27].

In OP2, further adjustments optimized the system's diagnostic capabilities. The image guide for coherence imaging spectroscopy (QRI) [26] was moved from AEF30B to AEF30A, while AEF30B was fitted with a fiber-optic bundle for the high-resolution spectrometer diagnostic (QSS) [27]. The AEF31 system was decommissioned, as its observation capabilities were replaced by an endoscope [24]. Finally, AEF41B was allocated to the real-time video diagnostic (QSV) [28].

These adaptations reflect the continuous evolution of diagnostic systems to meet the operational and experimental needs of W7-X. Table 2 gives an overview of the filter and system location during the operational phases.

2025 JINST 20 T04003

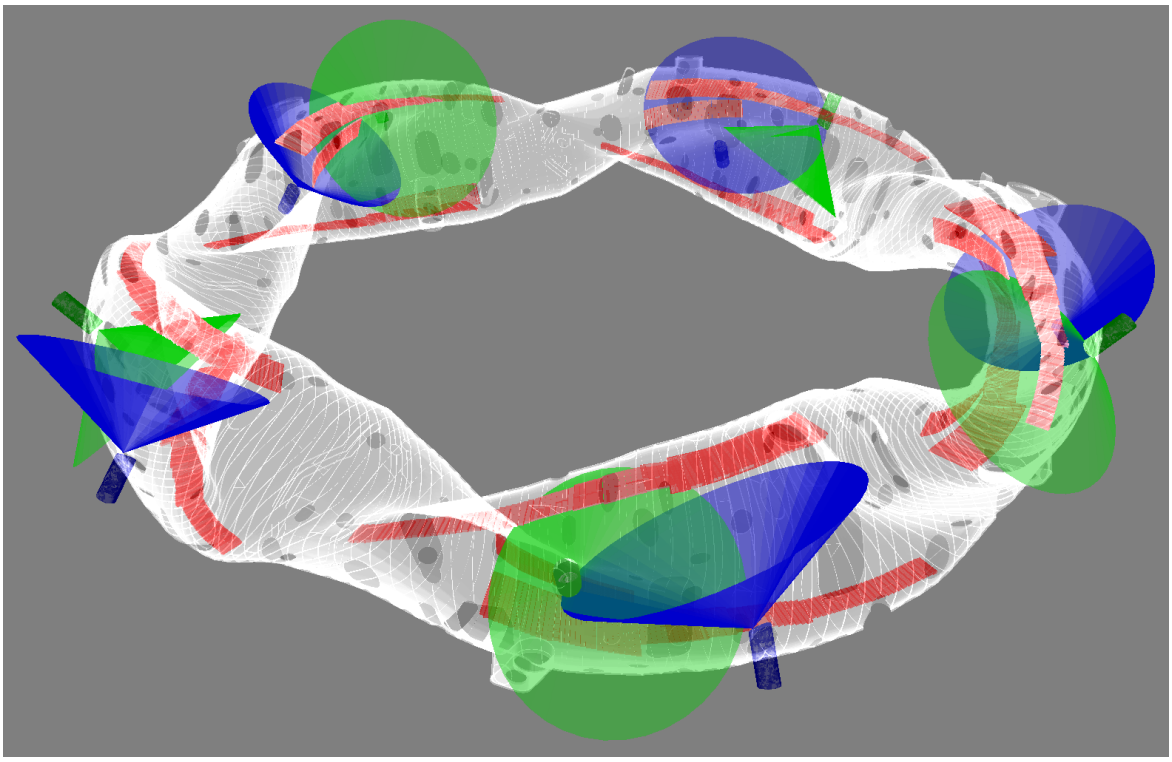

Figure 1. Field of view cones. The AEFX0 (green) and AEFX1 (blue) cameras field of view covering the divertor targets (red) in each module of W7X.

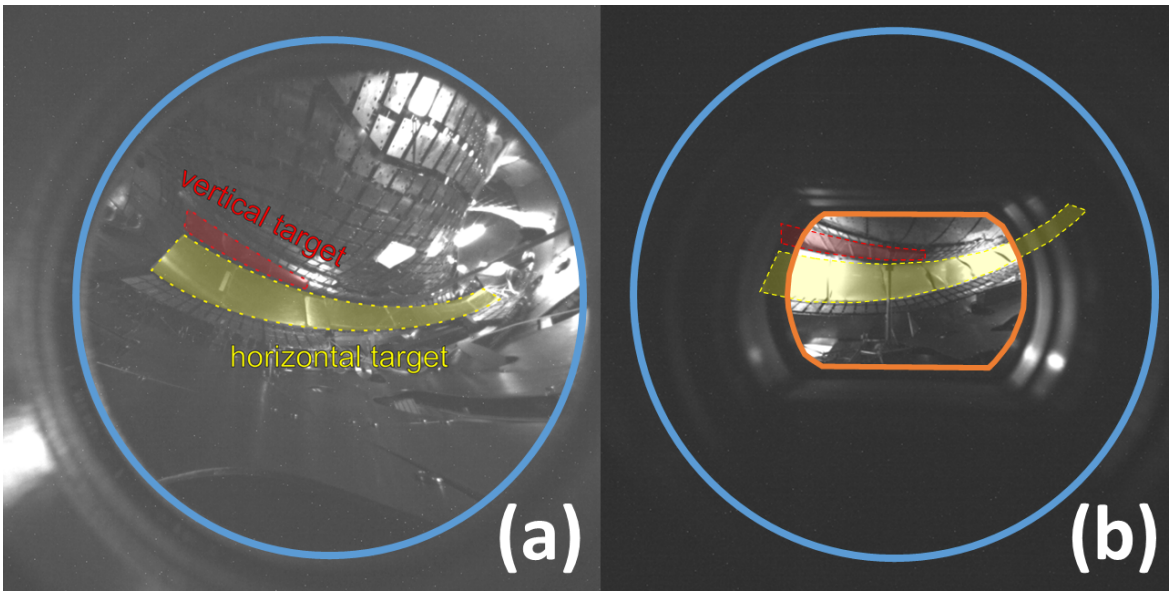

Figure 2. Sample fields of view. (a) The horizontal (yellow) and vertical (red) divertor targets, along with the surrounding baffle, are fully covered by the FOV. Fractions of the heat shield and steel panels are also visible. (b) After the hardening modifications for HE2, the observable area has been reduced, as shown: the original FOV (blue) compared to the OP2 FOV (orange). Small sections in the low-iota region on the left and the high-iota tail section on the right of the horizontal target are no longer within the FOV.

2025 JINST 20 T04003

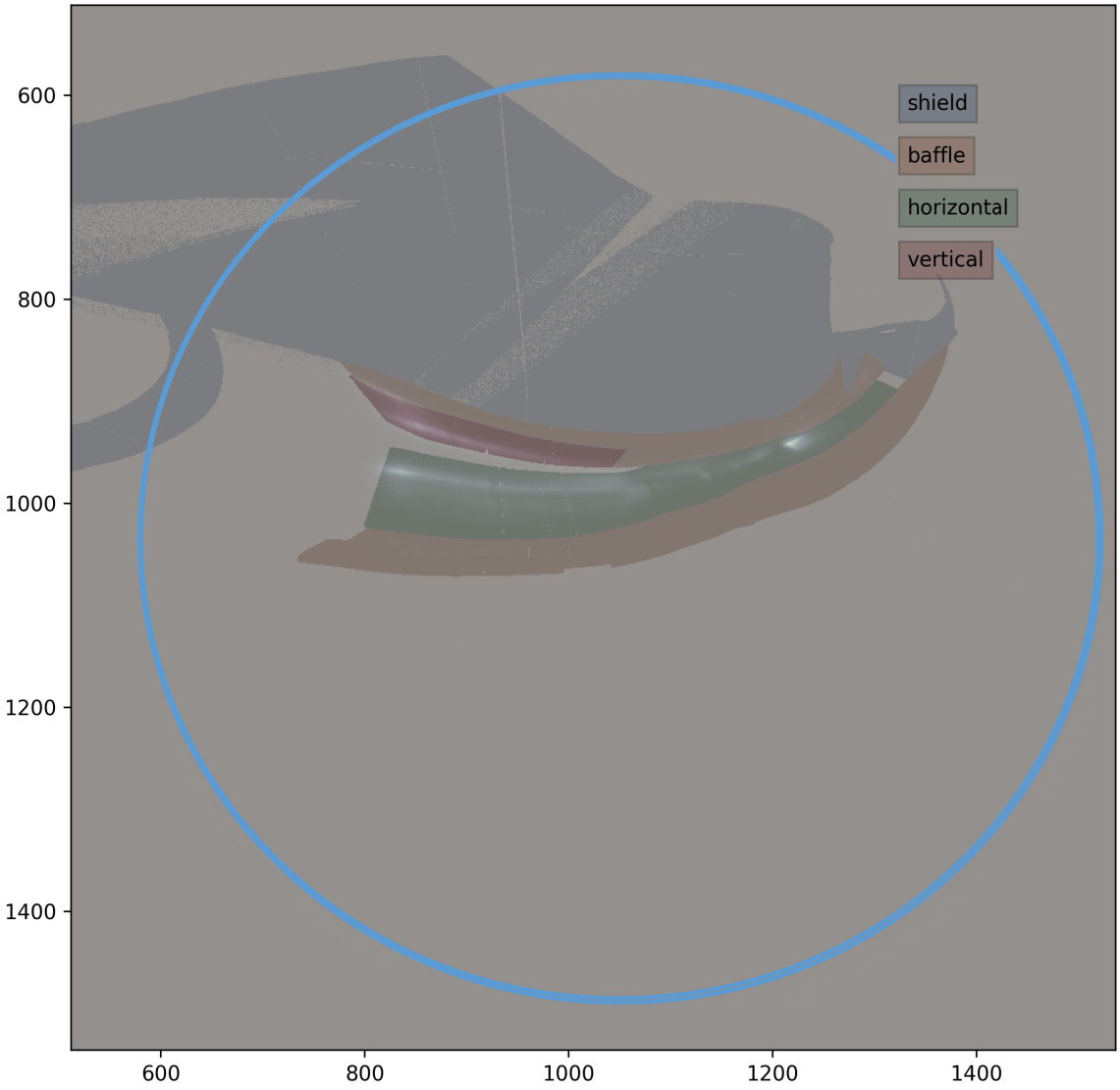

Figure 3. Calibrated sample image. A fully calibrated camera image of camera 11A from program ID 20181010.010 at 4.16 s. The H_α photon flux measurement is laid over the PFC locations of the horizontal (green) and vertical (red) divertor target, the baffle (yellow), and the heat shield (grey) in the scene model. The FOV of the camera is shown as a blue circle.

3.1 Immersion tubes: protection in harsh environments

The immersion tube is a critical component designed to protect cameras and facilitate their operation in the harsh environment of the W7-X plasma vessel. The system meets stringent requirements for UHV, thermal management, magnetic compatibility, and structural integrity while ensuring reliable diagnostics at atmosphere environment.

The immersion tube serves as a vacuum barrier and is constructed from a welded steel cylinder, weighing approximately 80 kg. The steel grade 1.4429/X2CrNiMoN17-13-4 is selected for its low magnetic permeability ($\mu_r < 1.01$) and its compliance with activation limits in neutron-rich environments, featuring cobalt concentrations below 2000 ppm. Magnetic shielding is intentionally

2025 JINST 20 T04003

Table 2. Filter and system allocation during the different operational phases.

Location	OP1.1	OP1.2a	OP1.2b	OP2
AEF10A	H_α	H_α	H_α	H_α
AEF10B	Open	H_γ	C-III	C-II
AEF11A	H_α	H_α	H_α	H_α
AEF11B	Open	C-III	C-III	C-II
AEF20A	H_α	H_α	H_α	H_α
AEF20B	C-III	C-III	H_γ	H_γ
AEF21A	H_α	H_α	H_α	H_α
AEF21B	C-III	H_γ	H_γ	H_γ
AEF30A	Open	H_α	H_α	QRI
AEF30B	Open	QRI/QSS	QRI/QSS	QSS
AEF31A	H_α	H_α	H_α	-
AEF31B	Open	H_α	H_α	-
AEF40A	H_α	H_α	H_α	H_α
AEF40B	Open	C-II	C-II	He-I
AEF41A	H_α	H_α	H_α	H_α
AEF41B	Open	C-II	H_γ	QSV
AEF50A	H_α	Prototype	Prototype	H_α
AEF50B	C-II	Endoscope	Endoscope	H_γ
AEF51A	H_α	H_α	H_α	H_α
AEF51B	C-II	QSS	QSS	QSS

Note: the filter change for OP1.2b was carried out in the last campaign week on 15.10.2018. For most of the campaign prior to this date, the allocation remained the same as OP1.2a. Filters for spectral lines of H_α - 656.3 nm, H_γ - 434.0 nm, C-II - 514.5 nm, C-III - 465.0 nm, and He-I - 667.8 nm, were utilized. Other diagnostics are abbreviated according to W7-X standard as follows: coherence imaging spectroscopy [26] - QRI, divertor spectroscopy [27] - QSS, and real-time video diagnostic [28] - QSV.

excluded to prevent interference with the plasma-confining magnetic topology. The vacuum interface is implemented using a rotatable vacuum flange similar to a DN300CF.

Optical access is provided through three soldered vacuum windows: sapphire for the two visible cameras and Zinc Selenide (ZnSe) for the IR observation. A pneumatically driven rotatable shutter protects the windows during wall conditioning procedures, such as boronization. The windows enable the placement of up to three cameras in proximity to the plasma. The visible cameras are positioned as follows, as shown in figure 4:

- 'A' (right hand side facing towards the plasma)
- 'B' (left hand side facing towards the plasma)

To mitigate thermal stress, the immersion tube is equipped with a pressurized air cooling system (figure 5). The pressurized air is supplied by the W7-X infrastructure in the torus hall. This cooling system reduces the operating temperature of the vacuum windows and cameras but does not entirely eliminate the risk of overheating. The system includes IR Camera Cooling with an

2025 JINST 20 T04003

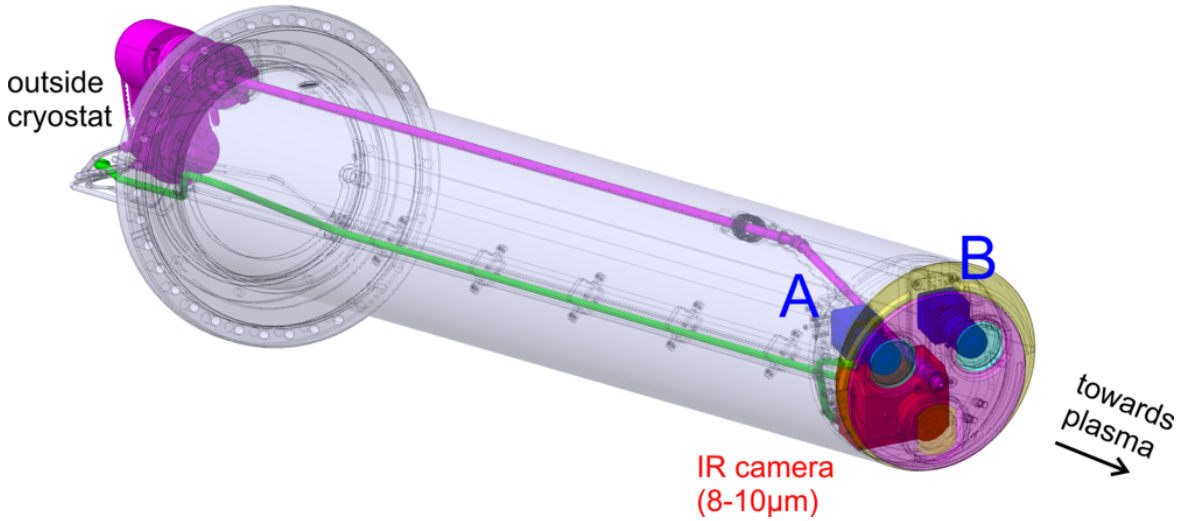

Figure 4. Immersion tube setup. The immersion tube is equipped with an IR camera (red) and two visible cameras (blue). The vacuum windows (light blue and yellow) are shielded by a rotating shutter (purple). A pressurized air line (green) provides cooling air.

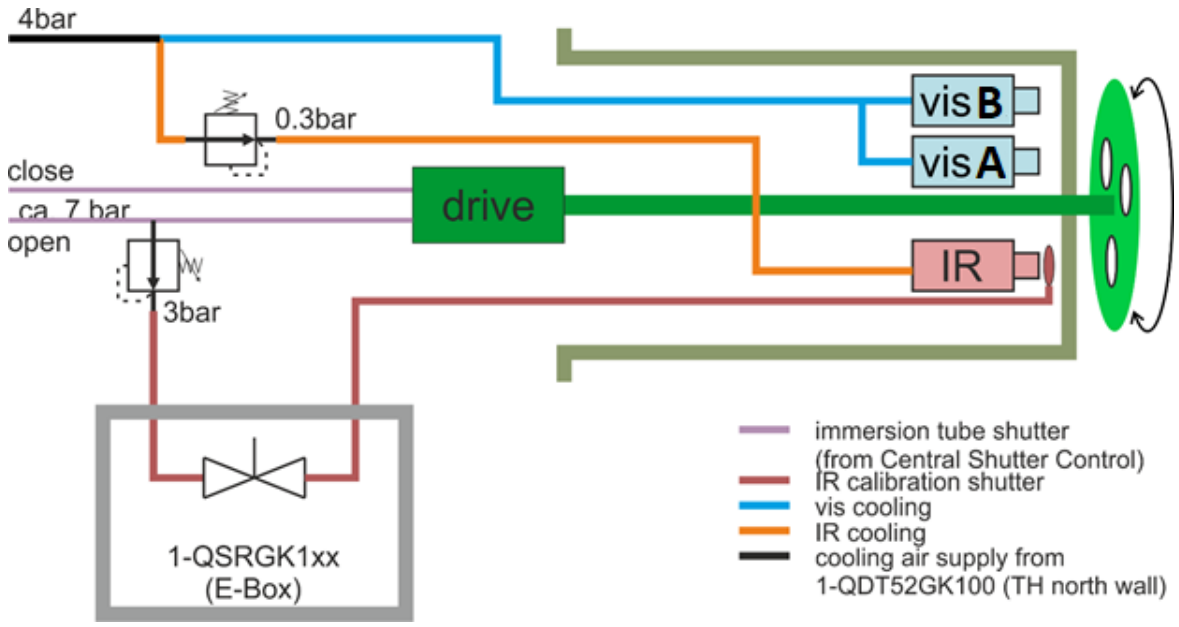

Figure 5. Cooling infrastructure in OP1. Pressurized air diagram for the immersion tube in OP1. Each immersion tube has two incoming air lines. A cooling air line at 4 bar and a control air line at 7 bar.

air flow at 0.3 bar and Visible cameras cooling with an air flow at 4 bar, directed along the camera casings and vacuum windows.

Despite air cooling, critical temperatures were observed during OP1.2. ECRH stray radiation can enter the immersion tube through the windows and lenses. A microwave resonator model predicts a heat load of up to 700 W/m^2 in the immersion tube. Combined with the cameras' thermal dissipation power (<2.9 W), this can raise camera temperatures beyond their operational limit of 55 °C.

2025 JINST 20 T04003

Figure 6 depicts the fastest temperature increase measured by a type N thermocouple near a sapphire window in module AEF10, where an ECRH injection in module 1 caused a rise of 1.6 K/s, exceeding the window specification of 0.42 K/s. To safeguard the windows, these operational conditions were avoided.

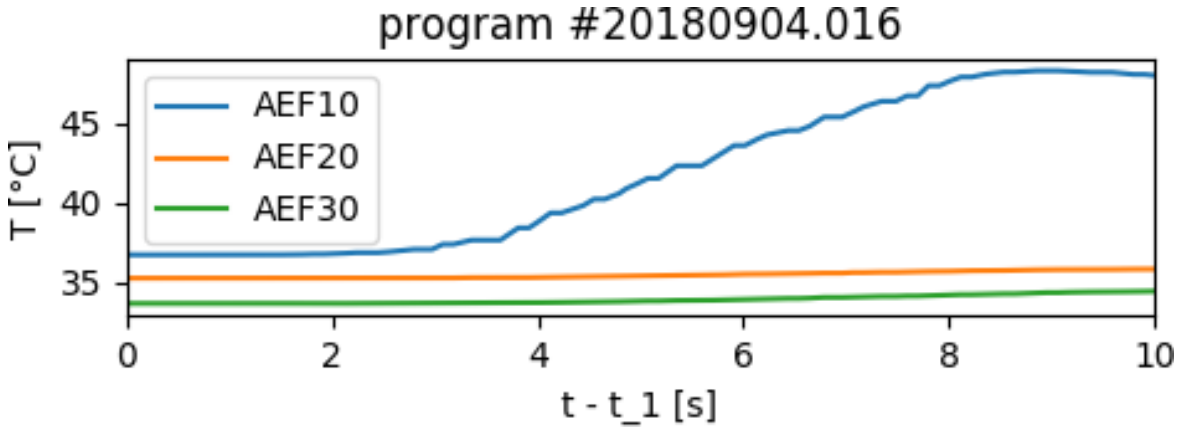

Figure 6. Temperature rise at vacuum windows. Fastest temperature rise observed during OP1.2 at AEF10, with ECRH injection causing a rise of 1.6 K/s, exceeding the window specification.

The immersion tubes can accommodate up to three cameras: two visible light cameras and one IR camera designed to measure the surface temperatures of PFCs [23].The cameras are mounted on a removable carriage, allowing hardware exchanges, such as filter replacements or aperture changes, within an hour. This modularity ensures adaptability between experimental days.

3.1.1 Hardening for long pulse operation in OP2

The transition from the inertially cooled test divertor unit (TDU) to the actively cooled high heat flux (HHF) divertor marked a significant milestone for W7-X, enabling long-pulse operations with increased energy input [29]. This shift introduces both opportunities and challenges, particularly in heat load monitoring and machine safety. While the HHF divertor's water cooling system supports higher power loads, it also increases vulnerability to damage, which could result in severe consequences from water leakage, such as the premature termination of the experimental campaign and lengthy repair periods, compared to the more robust TDU [30]. Machine safety, second only to personal safety, remains paramount.

At the start of OP2, only two endoscopes were operational. Thus, the immersion tube system, initially developed for HE1, remains indispensable for monitoring the heat loads on the remaining eight divertor units via IR cameras. To meet the demands of HE2, the immersion tubes were upgraded to ensure reliable heat load surveillance without compromising the vacuum safety of W7-X.

To protect the vacuum barrier, specifically the vacuum windows and sensitive weld seams, and to protect the cameras from thermal overload, a series of enhancements were introduced. The hardened immersion tube, as shown in figure 7, exemplifies these improvements. It features a 3D-printed graphite-covered cooling plate, along with integrated cooling water lines.

Plasma Radiation Protection:

- A protective front plate made of graphite was installed to absorb plasma radiation and act as a heat buffer for the more heat-sensitive steel plate underneath. Graphite was chosen due to its

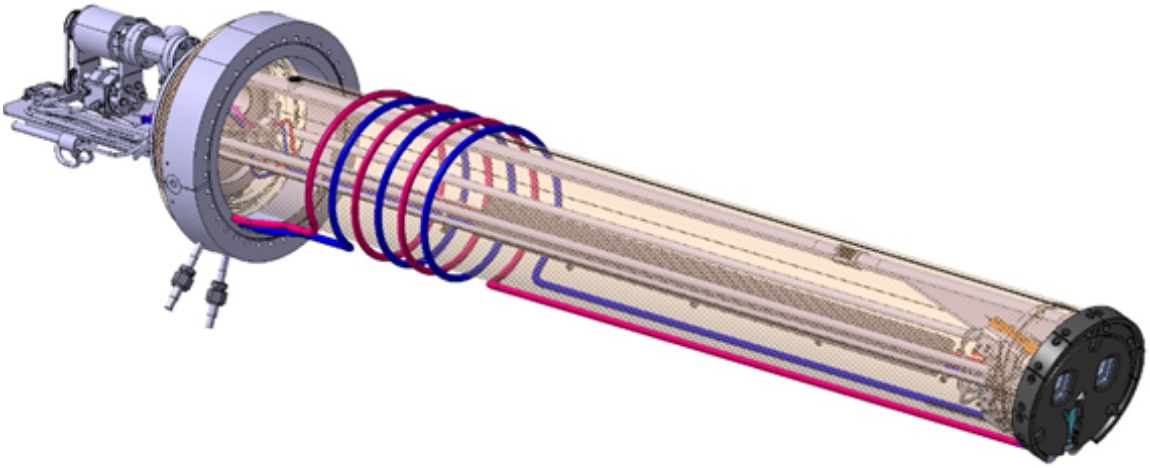

Figure 7. Hardened immersion tube. Immersion tube equipped with 3D printed, graphite covered, cooling plate. Cooling water feed line in blue with the return line in magenta.

high maximum temperature tolerance of 1200 °C. Additionally, a shootingstar-shaped cut-out in the graphite plate was used to reduce imparted energy on the ZnSe window.

- A water-cooled plate made of stainless steel, which can withstand temperatures up to 350 °C, was designed to transfer the absorbed heat into the water through 3D-printed integrated cooling channels, as showcased in figure 8.

- Protective sapphire windows, 8 mm thick, were embedded into the water-cooled plate, effectively decoupling the heat protection function from the vacuum windows. This design choice prevents plasma-induced damage to the vacuum barrier, while optimizing heat management. Additionally, temperature sensors were installed on critical components to monitor and manage heat buildup during operation.

ECRH Stray Radiation Protection:

- The protective sapphire windows were treated with an IMITO-coating (index-matched indium tin oxide) with surface resistance $< 20\,\Omega/m^2$, to reflect 98 % ECRH stray radiation. This coating, applied to the back side of the windows to prevent arcing, ensures high stray radiation reflection while allowing effective heat management. However, this design results in the stray radiation being absorbed twice by the window, with an absorption coefficient of $\alpha = 0.01$.

- To address the exposure of cameras to ECRH stray radiation, which primarily affects the plastic materials used in their construction, microwave reflection sheets made of aluminum were applied, depicted in figure 9. These sheets reflect stray radiation and help keep the camera temperatures within safe limits (electronics limit = 70 °C).

- To prevent heat buildup over time, the microwave reflection sheets are connected to water-cooled heat sinks that transfer the heat away from the cameras, depicted in figure 10. The updated pressurized air and cooling water layout can be seen in figure 11.

2025 JINST 20 T04003

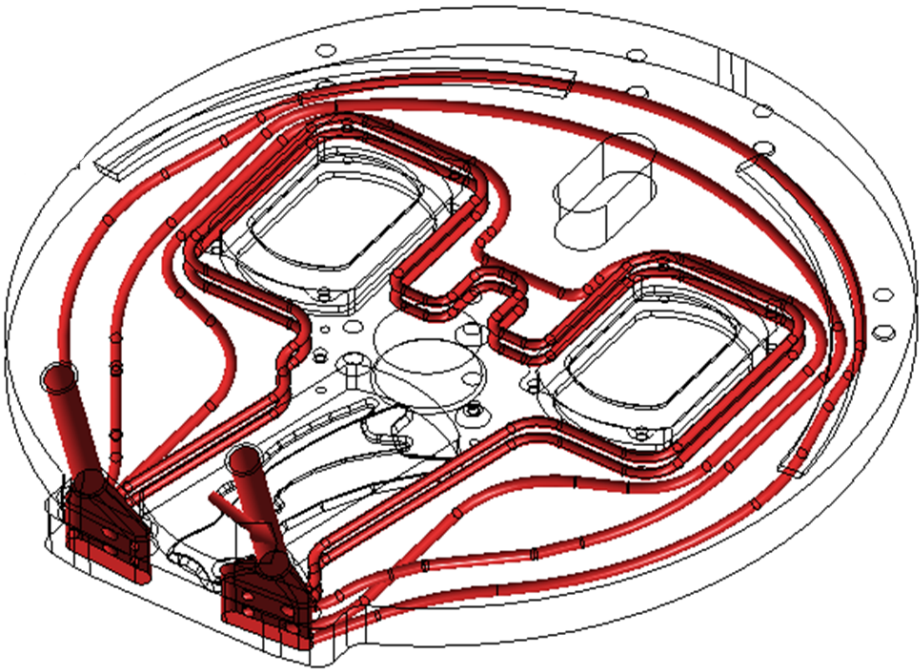

Figure 8. Integrated 3D printed cooling channels. The integrated cooling channels are highlighted in red inside the contours of the 3D-printed steel plate.

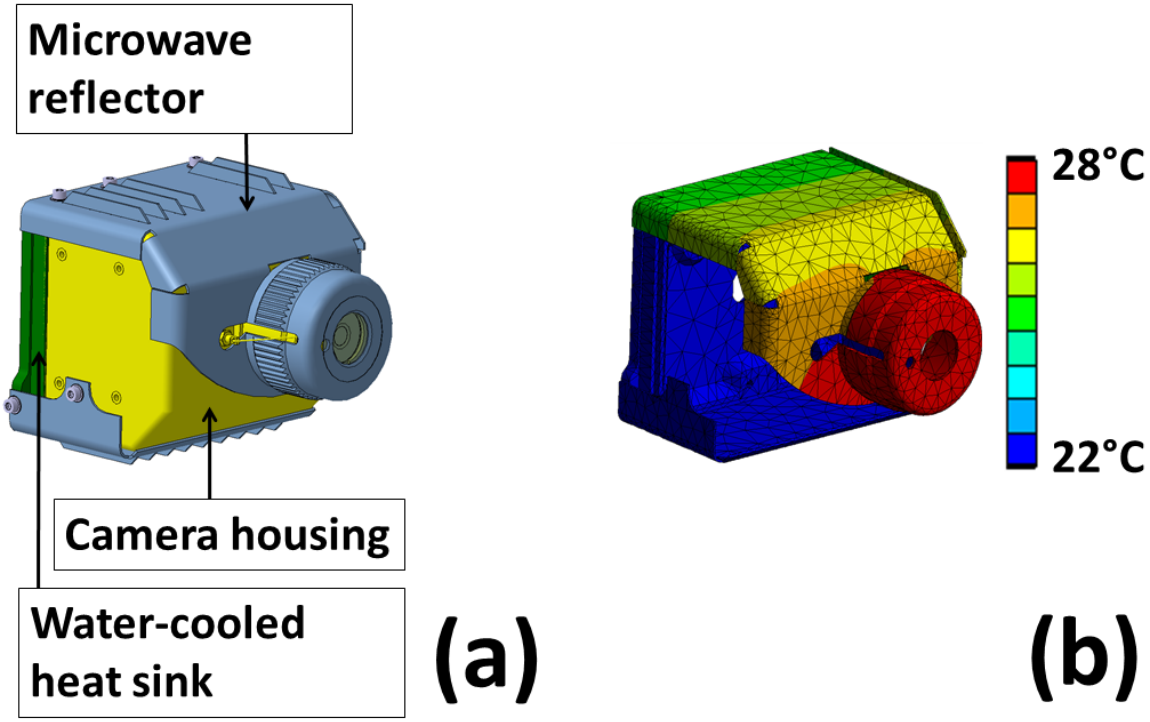

Figure 9. ECRH reflection sheets. (a) ECRH reflector sheets (grey), water cooled heat sinks (green) surround camera housing (yellow). (b) Temperature simulation of reflector sheet with HE2 loads between 22 °C and 28 °C.

2025 JINST 20 T04003

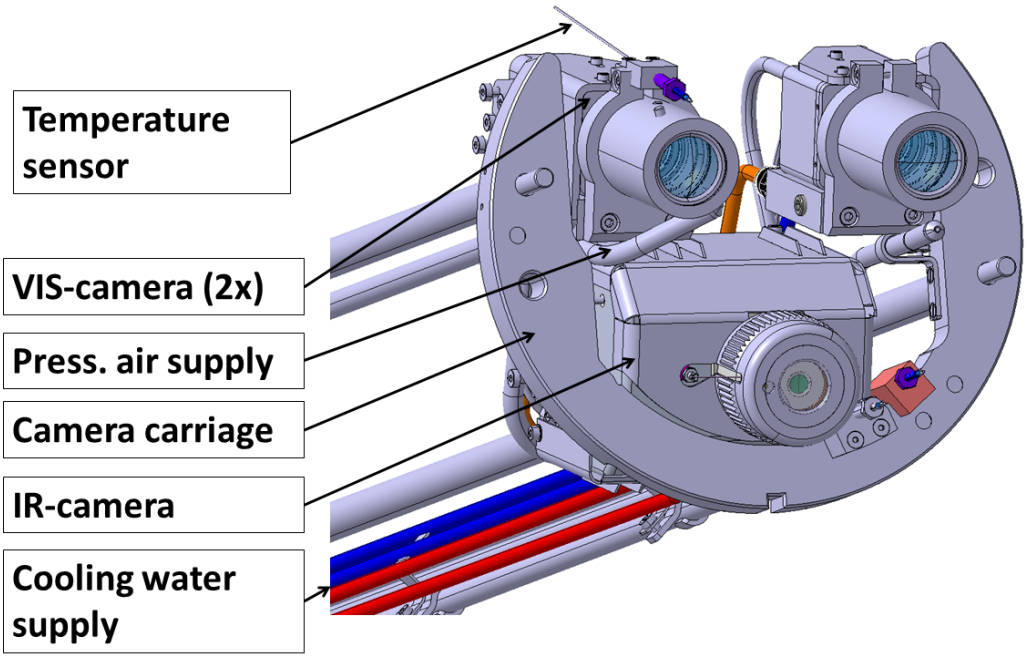

Figure 10. Hardened camera assembly in camera carriage. Cameras equippided with ECRH reflector sheets and water cooled heat sinks assembled in the camera carriage with air and water cooling (red/blue) infrastructure.

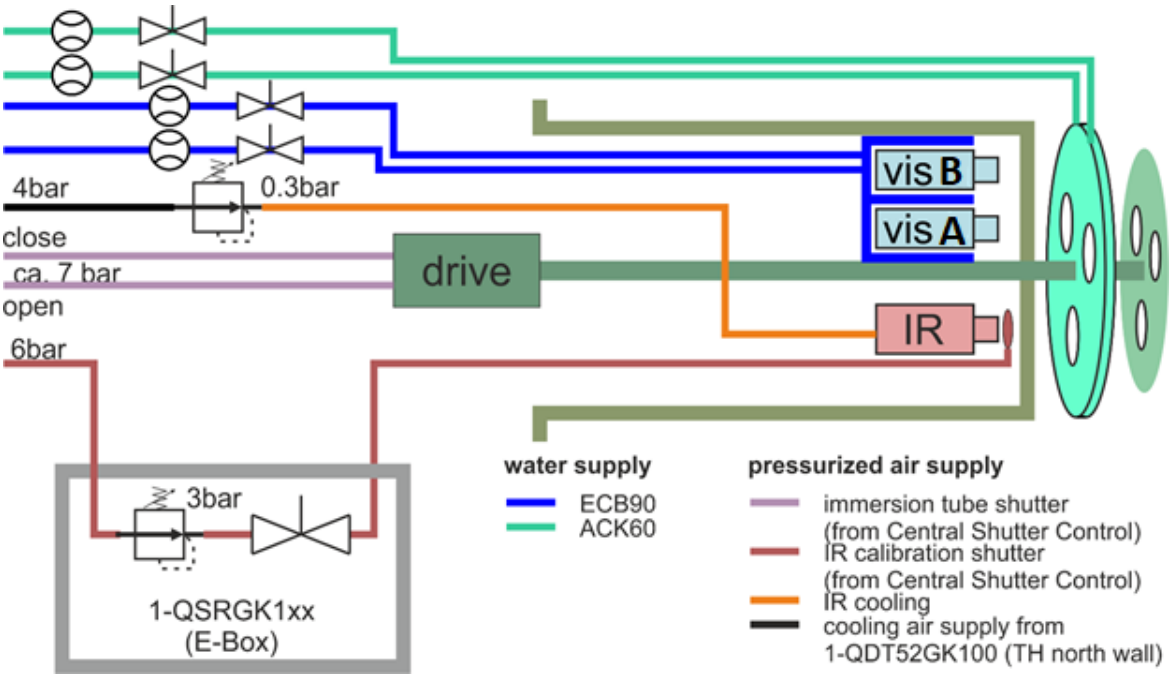

Figure 11. Cooling infrastructure in OP2. Pressurized air and cooling water diagram for the immersion tube in OP2. Each immersion tube has three incoming air lines and two incoming water lines.

]

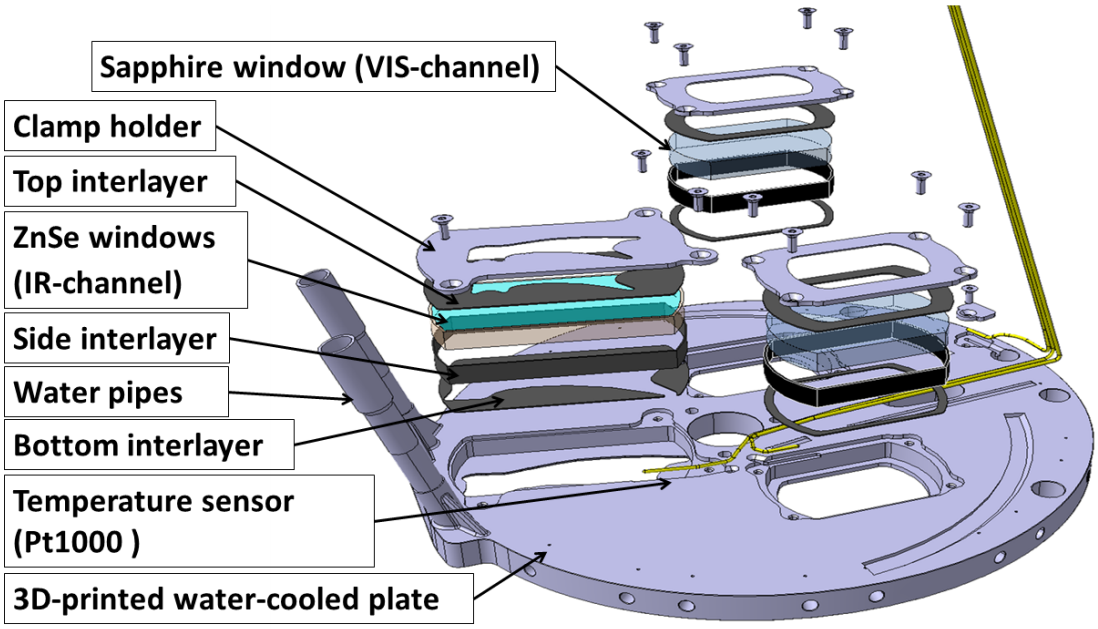

Figure 12. Exploded view window assembly. This view highlights the assembly of protective windows, including interlayers and holders. An integrated temperature sensor (yellow) is also part of the design.

Fast Particle Loss Protection:

- The steel collars previously used to protect against fast particle losses from neutral beam injection were replaced with graphite collars, offering improved thermal resilience and compatibility with HE2.

The additional design considerations for the immersion tube system aim to ensure component survival during HE2 while addressing inherent challenges. The 3D-printed water-cooled plate offers significant geometric flexibility, enabling the integration of intricate cooling channels within a compact design. This innovation eliminates the need for manual welding, thereby reducing error risks and enhancing overall reliability. Nevertheless, 3D printing introduces higher surface roughness, potentially compromising vacuum compatibility [31]. Furthermore, thermal deformation and reduced accuracy necessitate post-processing to achieve functional surface standards.

The IMITO coating, applied to protective windows, reflects 98 % of ECRH stray radiation. While the coating minimizes the ECRH load inside the immersion tube, quality assurance poses challenges, as direct surface resistance measurements are not feasible. To prevent arcing during wall conditioning procedures, the coating is applied to the window's backside, resulting in double absorption of radiation and increased thermal loads on the protective windows. To manage this, the windows are mounted with a graphite based Sigraflex interlayer, improving heat conduction, as depicted in figure 12.

Diagnostic positioning challenges have also been addressed during the upgrades. For example, immersion tubes AEF10 and AEF51 are located near the ECRH launcher and opposite reflective wall tiles. This positioning risks direct rays striking the diagnostics, necessitating additional bolometers in these tubes for stray radiation monitoring during OP2.

2025 JINST 20 T04003

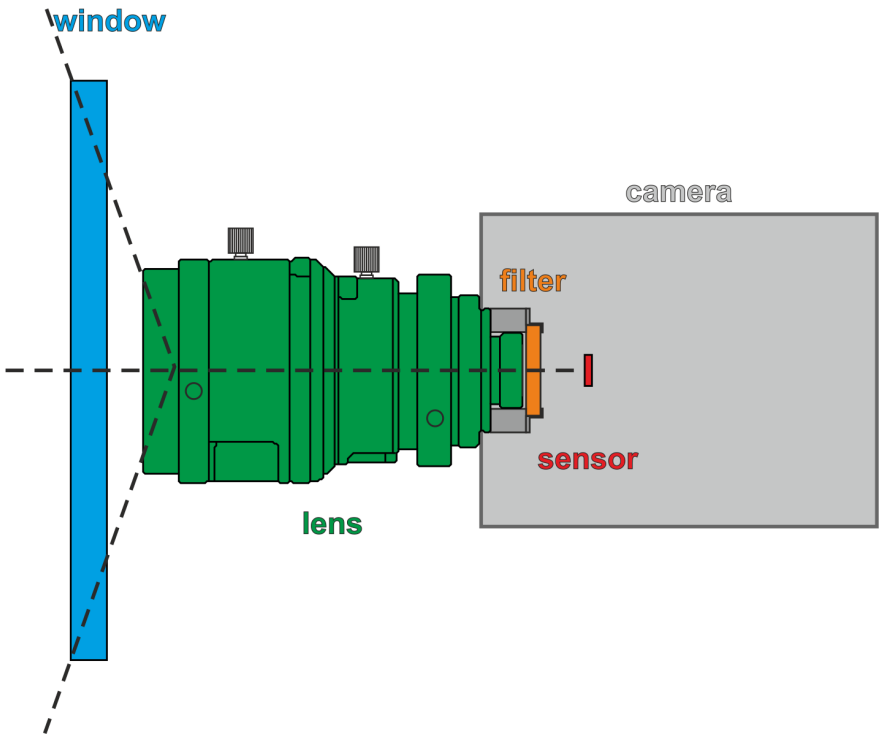

Figure 13. Optical path. The general optical setup for each camera system with a visible light sensor (red) housed in a camera (grey). The setup includes a wide-angle lens (green) positioned behind a sapphire vacuum window (blue). A band-pass filter (orange) is mounted on the rear of the lens.

These enhancements ensure the immersion tube system operates reliably under HE2's demanding conditions while safeguarding W7-X's safety and structural integrity. However, the 3D-printed plate has reduced the FOV of visible cameras, decreasing the usable image area by 82 %, as shown in figure 2. Consequently, the horizontal divertor target modules eight and nine, known as the high iota tail, fall outside the FOV.

3.2 Optical path from the plasma to the sensor

Before plasma light can be detected by the scientific complementary metal-oxide-semiconductor (sCMOS) sensor, it traverses several optical elements, including a sapphire vacuum window, a wide-angle lens, and a narrow band-pass optical filter. The general optical path is depicted in figure 13, with the object plane on the left. IR light, on the other hand, passes through a ZnSe vacuum window and a lens integrated within the camera before being captured by the microbolometer sensor. The thermal protection windows added in the hardening process are of 8 mm thickness and are fabricated to the same specifications as the respective vacuum windows.

3.2.1 Windows

The sapphire window serves as a thermal protection and vacuum barrier for the visible cameras, optimized for a wavelength range of 350–800 nm. It ensures high precision with a parallelism of less than 3 arc minutes and a surface finish of 50/20 Scratch-Dig, while maintaining a surface roughness (Rq) below 3 nm. The transmitted wavefront error (TWE) is controlled to a power of less than 8λ and

2025 JINST 20 T04003

an RMS of less than 4λ. This window operates effectively in a thermal range from 0 °C to 350 °C, with UV transmission exceeding 50 % at 350 nm. To enhance durability and usability, the edges are deburred to a precision of $0.1 \pm 0.1 \times 45°$ or rounded to $R = 0.1$.

The ZnSe window is employed for the IR cameras, specifically optimized for a wavelength range of 8–10 µm. It offers high accuracy with parallelism below 3 arc minutes and a surface finish rated at 40/20 Scratch-Dig, complemented by a surface roughness (Rq) under 3 nm. Its transmitted wavefront error (TWE) is limited to a power of less than 8λ and an RMS of less than 4λ, ensuring precise optical performance. This window is designed to withstand temperatures ranging from 0 °C to 200 °C and includes edge treatments to eliminate sharp edges, deburred to $0.1 \pm 0.1 \times 45°$ or rounded to $R = 0.1$. An anti-reflective coating for the 8–10 µm range is applied to one side.

3.2.2 Wide angle lens

The cameras are equipped with 135° wide-angle lenses of type MY125M by Theia Technologies [32]. These lenses are characterized by high light intensity, offering a focal length of 1.3 mm with an aperture of 1.8. They are optimized for sensor sizes ranging from $\frac{1}{3}''$ to $\frac{1}{2.5}''$, meaning the outer frame of the $\frac{2}{3}''$ sensor is not illuminated, as discussed in section 4. Additionally, the lenses originally featured an iris aperture made of magnetizable metal, which was replaced after operation phase OP1.2a with a brass foil containing a fixed-size hole (see section 6).

3.2.3 Filter

Filters are positioned between the camera and lens, as depicted in figure 13. These filters are made of unmounted glass with a thickness of 2 mm and a diameter of 12.5 mm. Five different types of band-pass filters have been utilized, each specified for a different spectral line, as detailed in table 3. The transmission curve of each filter was measured, and calibrations were performed to account for the effect of non-normal incident light. Since the light rays converge at the filter's location, a shift in the filter transmission curve must be considered, as discussed in section 4.

Table 3. Specifications of band-pass filters.

Line	Manufacturer	CWL [nm]	FWHM [nm]	OD
H_α	Alluxa	656.2	1.5	OD6
H_γ	Alluxa	434	2	OD4
He-I	Alluxa	667.8	2	OD4
C-II	Semrock	514	2	OD4
C-III	Alluxa	465	2	OD4

Note: overview of band-pass filters used for the spectroscopic cameras, with the specified center wavelength (CWL), full width at half maximum (FWHM), and blocking in the 200–1200 nm range at the given optical density (OD) level.

3.2.4 Cameras

The visible cameras, of type "Cygnet 4K" sCMOS manufactured by Raptor Photonics Ltd., capture 2048×2048 pixel frames at a rate of 25 Hz. The $\frac{2}{3}''$ sCMOS sensor is optimized for high sensitivity, featuring a pixel pitch of 5.5 µm, a spectral response range from 350 nm to 1100 nm, and a peak quantum efficiency of 63 % at 500 nm. With readout noise below 12 electrons and a dynamic range of

2025 JINST 20 T04003

60 dB, these cameras provide excellent performance. However, their 12 bit bit depth requires constant exposure adjustment to match the varying plasma conditions during experiments. Exposure times can be set from 27.7 µs to 1/framerate. Occasionally, irregular saturation effects due to interference between the TTL trigger and integration time were observed at short integration times, as further elaborated in section 6. The cameras consume less than 2.9 W and operate within a temperature range of −20 °C to 55 °C.

The IR cameras, custom-built for operation in high magnetic fields, are of type "Caleo 768k L" by IRCAM. They record 1024 × 768 pixel frames at rates up to 120 Hz. Equipped with microbolometers featuring a 17 µm pixel pitch, these cameras have a spectral response range of 8 µm to 14 µm. Their analog-to-digital resolution is 14 bit, with a Camera Link data interface operating at 24 bit and 75 MHz. Exposure times range from 0.5 µs to 9.72 µs. These cameras are operational within a non-condensing relative humidity range of 20 % to 80 % and a temperature range of 0 °C to 50 °C. The integrated lens provides a horizontal FOV of 116°.

3.3 Data acquisition

The data acquisition (DAQ) system is distributed across three primary locations, dictated by cable length constraints and resilience to magnetic fields. Components resilient to strong magnetic fields are installed within the immersion tube itself (see subsection 3.1). Components sensitive to magnetic fields but requiring cable lengths shorter than 7 m are housed in electrical boxes (e-boxes) located within the torus hall. These e-boxes primarily contain power supplies and electro-optical converters for camera control and data signals. To address the limited space in the torus hall, reduce magnetic interference, and facilitate operational access, the majority of the DAQ infrastructure is situated in electrical cubicles approximately 100 m from the immersion tubes, outside the torus hall.

Originally designed and implemented by the diagnostic department for OP1, the DAQ system underwent a comprehensive upgrade and was transferred to the Control, Data Acquisition, and Communication (CoDaC) group in preparation for OP2 [33]. These upgrades optimized the system for enhanced integration and scalability, particularly for compatibility with the endoscopes that will rely on shared infrastructure. Below, the OP1 and OP2 configurations are detailed.

3.3.1 OP1: initial configuration

The DAQ system during operation phase OP1 is outlined in figure 14. Visible cameras were operated via Camera Link interfaces, receiving external frame clock signals over TTL triggers. Fiber optic cables transmitted these signals to seven electrical cabinets in the basement, where electro-optical converters reverted them to electrical signals. A single-board computer module (Red Pitaya) generated the triggers, which were multiplied for individual cameras using a FanOut module. This module synchronized with the central W7-X control system via a preparation trigger 1 min before each experiment, ensuring synchronous sensor exposure within 100 µs of plasma startup. This setup also captured dark images prior to plasma onset for background subtraction.

Camera signals were directed to dedicated DAQ PCs that managed camera settings, locally stored frames, and uploaded the data to the MDSplus database [34]. At the end of each experimental day, the data was transferred to the central W7-X archive for long-term storage and analysis [35].

2025 JINST 20 T04003

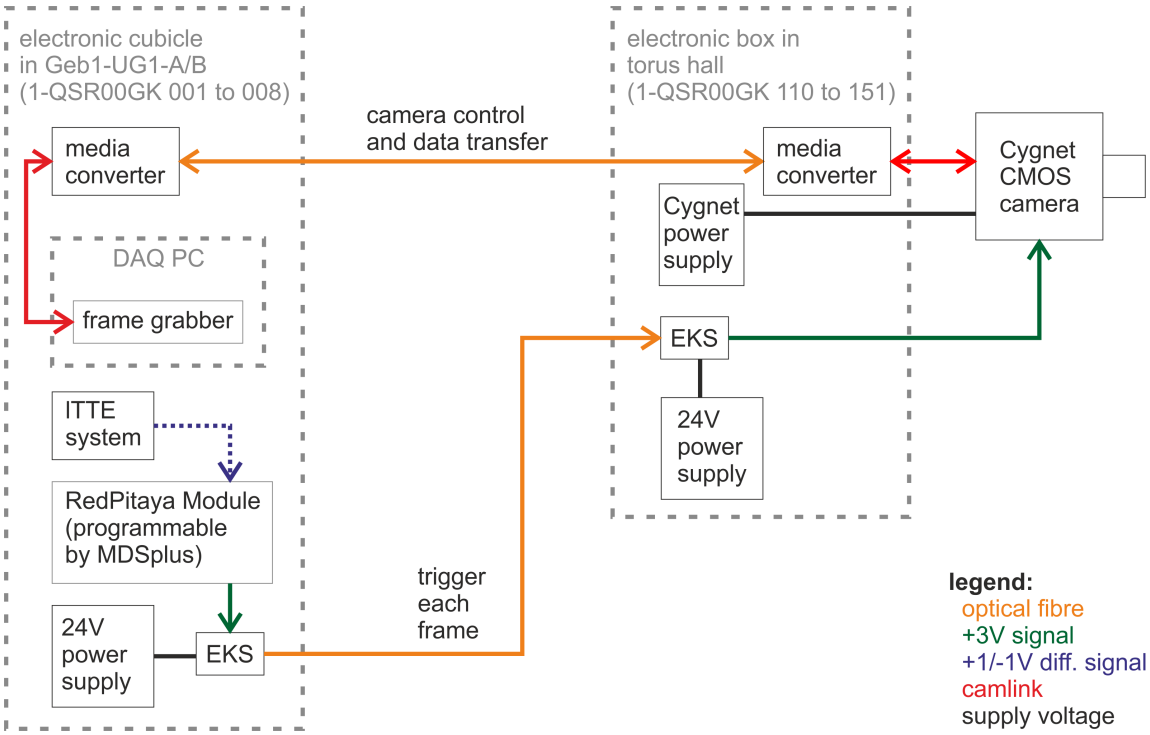

Figure 14. OP1 data acquisition flow diagram. DAQ flow diagram with camera control via Camera Link (red), frame trigger signals (green), fiber optic transmission (orange), and power supply (black).

3.3.2 OP2: CoDaC integration and advanced processing

From OP2.1 onward, the camera DAQ system is fully integrated into the W7-X CoDaC infrastructure. Cameras are connected to frame grabbers housed in MTCA4 crates, enabling real-time processing. Visible camera data is stored in the archive and displayed on visualization workstations, while IR camera data is processed in real time on module protection workstations (MPWS). These workstations apply temperature calibration and hotspot detection algorithms. Thermal event notifications can trigger hardware alarms via the fast interlock system, protecting the HHF divertor [30].

The DAQ system has been re-equipped with CoDaC compatible components changing the DAQ flow as depicted in figure 15. Trigger signals are now generated by TTE modules, providing independent frame clock triggers for each camera. Visualization workstations in the control room serve as interfaces for data monitoring, while programmable logic controllers (PLCs) provide remote access through VNC connections to WINCC graphical interfaces.

The DAQ system supports multiple camera models using fiber-based Camera Link connections, including Camera Link HS for pco.edge visible cameras in endoscopes and proprietary converters for other models. Custom-built W7-X adapters extract CC1 control line triggers for cameras requiring external triggering via SMA connectors.

To standardize hardware, W7-X CoDaC partnered with DMCS in Łódź to develop GenICam-compatible, transport-agnostic MTCA4 frame grabbers. These frame grabbers are interconnected with Dell PowerEdge R6515 servers via PCIe uplinks, enabling neural network-based image analysis. This configuration avoids reliance on the limited computational resources of MTCA blade CPUs and supports real-time processing of high-resolution image data.

2025 JINST 20 T04003

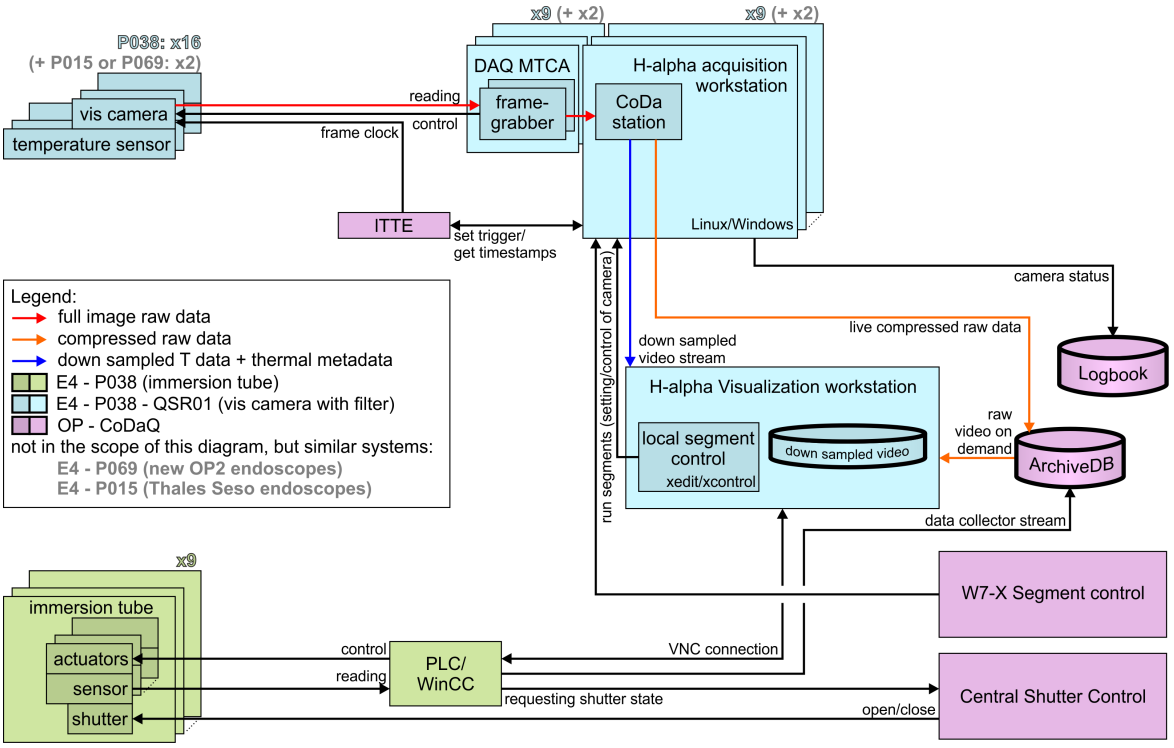

Figure 15. OP2 data acquisition flow diagram. Flow of full image raw data (red) from cameras to frame-grabber and CoDa stations. From there compressed raw data (orange) is stored in the archive, while down sampled data (blue) is streamed to visualization workstations in the control room.

Processed and raw data are compressed using the Fusion Power Video Codec, a specialized format co-developed with Google engineers. Compressed data is streamed directly to the W7-X archive and the W7-X DataMonitor system, which supports live visualization in the control room, office environments, and for remote team members via the W7-X ExtraNet.

4 System calibration

Precise calibration of the imaging system is crucial to reliably convert the raw digital levels (DL) recorded by each pixel into photon flux densities along the respective LOS. The signal intensity measured with the camera is determined by the camera position, optical system, line radiation filters, and sensor electronics. To extract a signal proportional to the incoming photon flux density, a step wise calibration of the images is required.

The calibration sequence starts with correcting for digital offsets and proceeds to account for optical and electronic influences, ultimately relating the photon emissions by the plasma along a LOS to the W7-X coordinate system. This ensures accurate mapping of absolute photon flux densities. The following subsections describe each step of the calibration process:

- Correction of Signal Offsets
- Correction of Bad Pixels
- Vignetting Compensation

2025 JINST 20 T04003

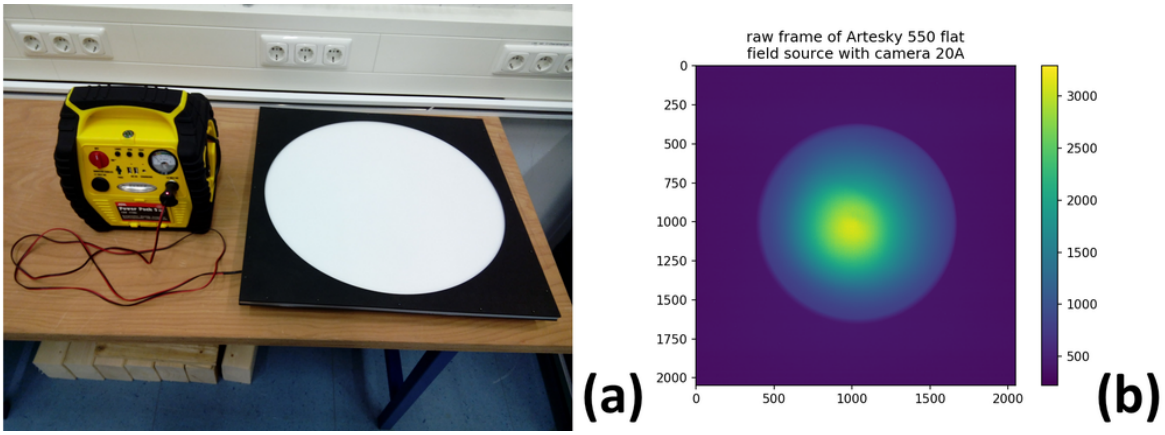

Figure 16. Flat field source and image. (a) Flat field source Artesky 550 with DC power supply. (b) Image of flat field source by camera 20A during tests in laboratory before operation phase OP1.2b with $t_{exposure} = 200\,\mu s$.

- Absolute Calibration to Photon Flux
- Filter Transmission Characterization
- Intrinsic Optical Model of the Camera
- Extrinsic Alignment to the W7-X Coordinate System
- Quantification of erosion and deposition on windows
- Inter-diagnostic comparison

4.1 Correction of signal offsets

The digital levels (DL) recorded by the sCMOS sensor include multiple sources of background signals, such as dark currents, thermal noise, and row-specific variations in reset voltages. These effects are observable even in pixels outside the imaging area, such as those at the image edges, which are unaffected by photons from the plasma. To accurately convert digital signals into photon flux densities, it is essential to correct these offsets on a per-image basis.

Experiments with an extended light source (see figure 16) confirm that the outermost 200 rows and columns of the sensor are not illuminated by observed light. Analysis of these edge regions reveals a structured line-pattern noise caused by row-specific offset variations (figure 17(a)). This offset pattern changes over time, requiring dynamic correction for each image.

To address this, the offset profile for each column is calculated by averaging the pixel intensities in the leftmost and rightmost 200 columns of the image (figure 17(b)). This averaged profile is then subtracted from the corresponding columns throughout the image. The residual pixel intensity variations in the edge regions provide an estimate of the digital noise level, which is used to determine the uncertainty in the corrected image. Typically, the offset magnitude is approximately 300 DL, while the residual noise uncertainty is about 8 DL. Once this offset pattern is subtracted, the corrected pixel signal exhibits a linear response to incident photons.

The photon flux density detected by the imaging system consists of contributions from plasma emissions and background sources. Background emissions are further categorized into ambient

2025 JINST 20 T04003

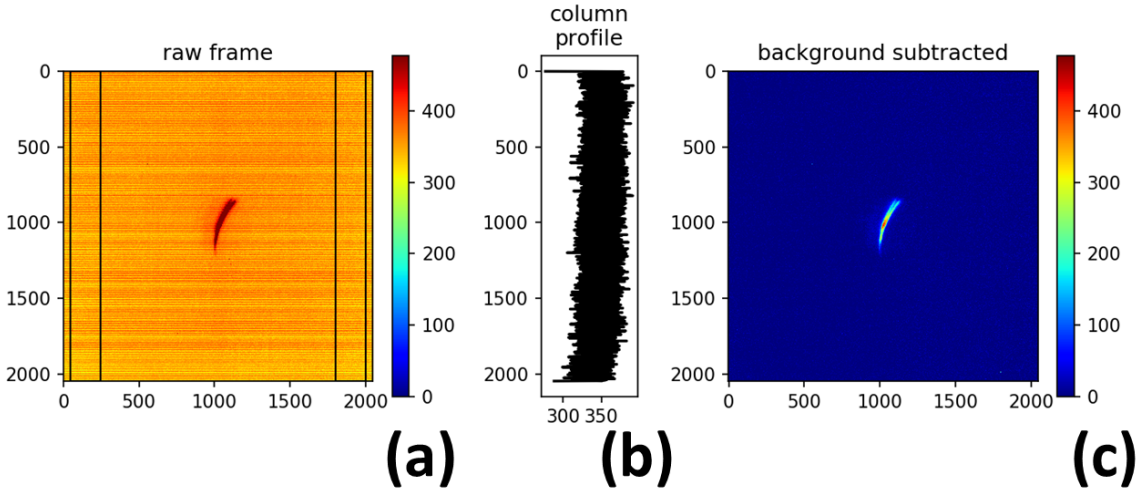

Figure 17. Background substraction. Example images of camera 20A from W7-X program #20171207.024. (a) Raw image from camera, (b) averaged column profile from left and right image edge, (c) image after background subtraction.

light and reflections. Ambient emissions, with a typical contribution of approximately 5 DL, are detected even with the shutter closed and are attributed to stray light inside the immersion tube. These ambient components are mitigated by subtracting an averaged frame captured from the empty plasma vessel before or after an experimental program.

Reflections from plasma-facing components (PFCs) represent another potential background source. These reflections, proportional to the plasma photon flux and the reflectivity of the PFCs, are assumed to be negligible due to the low reflectivity of graphite in the visible spectrum.

4.2 Correction of bad pixels

Flat-field images (figure 16(b)) and dark images, taken with a lens cap on, were analyzed to identify bad pixels in the sensor array. Bad pixels were defined as those whose intensity deviated significantly from the local pixel average, as determined by subtracting a blurred image using a size-9 boxcar filter from the original image. Pixels exhibiting deviations greater than three standard deviations from the local average were flagged as bad.

Analysis revealed sporadic, isolated bad pixels, with no clusters or patches. Furthermore, since the field of view is restricted to the central part of the sensor plane, bad pixels in the peripheral edge rows and columns were excluded from correction.

For each identified bad pixel, the intensity was replaced by the average of the four immediately adjacent pixels. This approach ensures that the correction preserves local intensity variations while mitigating the impact of anomalous pixel responses. The resulting images are thus free from spurious artifacts introduced by bad pixels, enabling accurate subsequent calibrations and analyses.

4.3 Vignetting compensation

The finite aperture of the lens system and the restricted opening of the vacuum windows contribute to a radial degradation in light acceptance as the distance from the optical axis increases. Collectively, these effects are referred to as vignetting.

2025 JINST 20 T04003

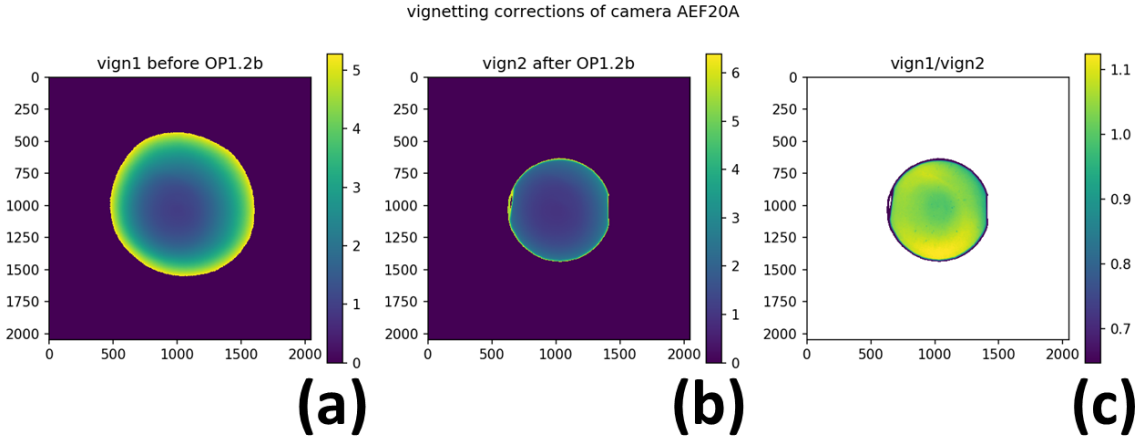

Figure 18. Vignetting comparison Example vignetting frames of camera 20A from before operation phase OP1.2b (a), after OP1.2b (b) and the ratio between these correction factors (c).

The vignetting effect was quantified using images taken of a uniform, extended flat-field light source (Artesky 550, figure 16). The images were first corrected for background noise and bad pixels. A set of six flat-field images was averaged and smoothed using a 5×5 boxcar filter to reduce noise. The ratio of the intensity at the image center, $I_{\text{flat field}}(x_c, y_c)$, to the intensity at each pixel $I_{\text{flat field}}(x_i, y_i)$, defines the vignetting correction factor:

$$f_{\text{vignetting}}(x_i, y_i) = \frac{I_{\text{flat field}}(x_c, y_c)}{I_{\text{flat field}}(x_i, y_i)}. \tag{4.1}$$

This correction factor is applied element-wise to the image intensities, effectively compensating for the radially varying light acceptance. The pixel-level fluctuations in $I_{\text{flat field}}(x_i, y_i)$ across the six images, combined with uncertainties in background subtraction, determine the relative uncertainty of $f_{\text{vignetting}}(x_i, y_i)$. These uncertainties vary by pixel, camera, and flat-field image quality.

The relative uncertainties in the vignetting correction factors, grouped by operational phases, are:

- Post-OP1.2a: $u(f_{\text{vignetting}}) \in [0.7, 13]\%$, mean $\overline{u} \approx 2\%$
- Pre-OP1.2b: $u(f_{\text{vignetting}}) \in [0.6, 3]\%$, mean $\overline{u} \approx 1.1\%$
- Post-OP1.2b: $u(f_{\text{vignetting}}) \in [0.3, 5]\%$, mean $\overline{u} \approx 1.1\%$

Applying the vignetting correction propagates its uncertainty into the overall measurement uncertainty.

Figure 18 illustrates vignetting correction factors derived from flat-field images before (a) and after (b) OP1.2b, and their ratio (c). The edge region outside the lens's imaging area is set to zero. After OP1.2b, the outer regions of the FOV exhibited reduced transmissivity.

Since vignetting effects can change over time, a time-weighted interpolation between pre- and post-operation calibrations is applied when both datasets are available. This assumes a linear transition of the vignetting pattern over the intervening period.

2025 JINST 20 T04003

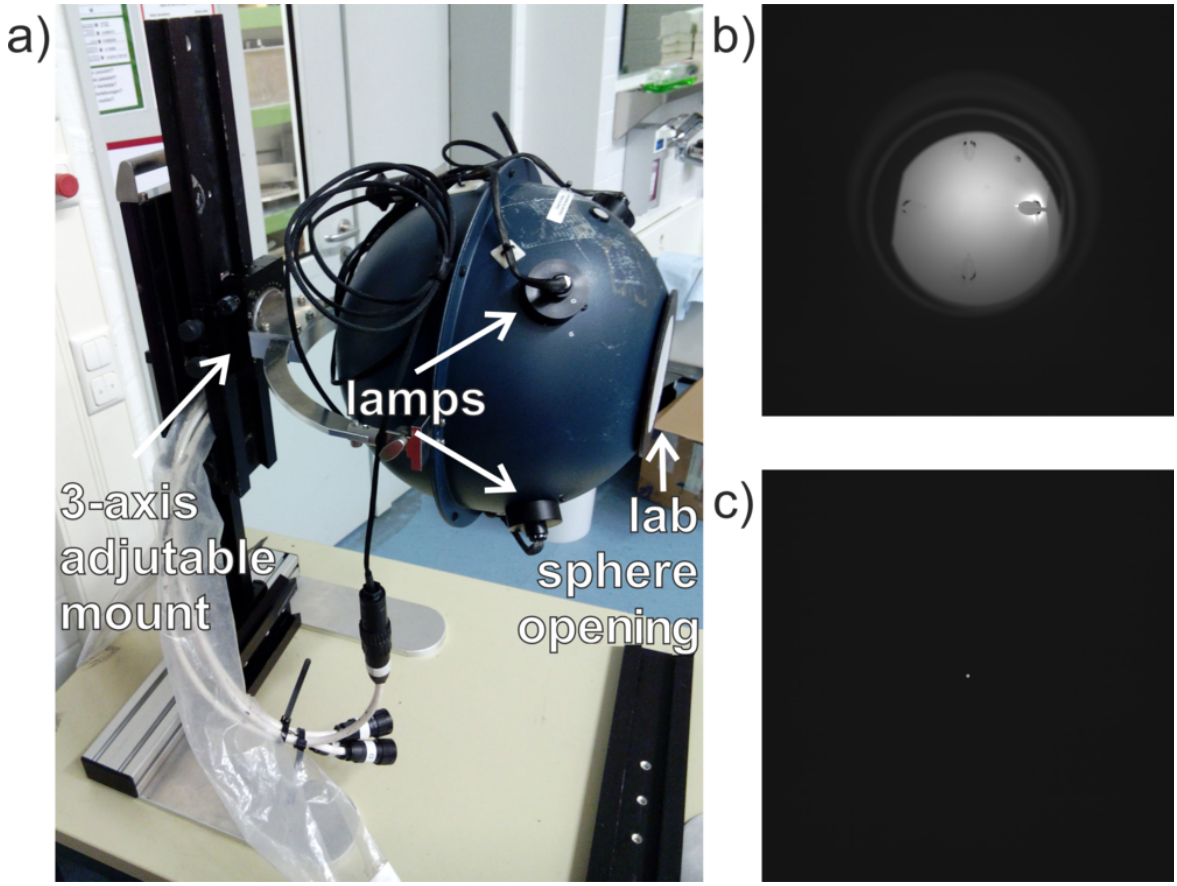

Figure 19. Absolute calibration setup and images. (a) Integrating sphere on an adjustable mount to align the opening normal to the camera view. Camera image (AEF10A) of integrating sphere opening (b) at close range and (c) at approximate later observation distance (1.5 m).

4.4 Absolute calibration

To convert the corrected digital signal into a physical property, images were captured of an absolutely calibrated light source: an integrating sphere (Ulbricht sphere) USS-1200 by Labsphere Inc. (figure 19(a)). This spherical cavity features four 30 W halogen light sources and a 12″ opening, with one halogen lamp (C) being sufficient for calibration. The lamp was powered by an LPS-045-H power supply providing regulated DC constant current ($I_{\text{lamp}} = 2.78 \pm 0.001$ A, $U_{\text{lamp}} = 11.85 \pm 0.03$ V).

At close range (figure 19(b)), the large opening of the integrating sphere filled the image. However, due to the lens's wide-angle view, the lamp shields were also captured, which prevented it from being used as a flat-field source for vignetting correction. At distances comparable to those used in W7-X experiments, the emitted light was nearly uniform, as shown by the relative luminosity profile in figure 20(a). The spectral radiance $L_{e,\Omega,\lambda}$ of the light source was measured by PTB Braunschweig in 2015 (figure 20(b)) and confirmed by a relative calibration using an HR4000 spectrometer from Ocean Insight (2016–2018). The integrating sphere is sent in regularly to PTB Braunscheig for re-calibration to ensure continous precision. Although the HR4000 and associated optical components were not absolutely calibrated, the spectral lines measured by the cameras showed relative variations of up to 1.3% between 2016 and 2018. This variation is included in the uncertainty of the spectral radiance.

2025 JINST 20 T04003

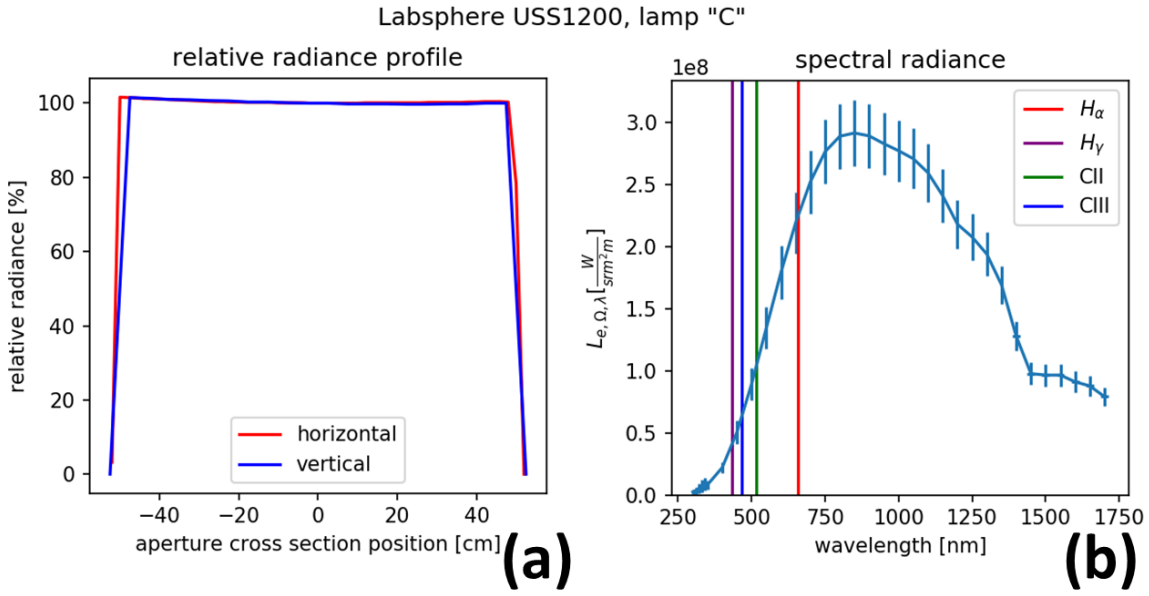

Figure 20. Integrating sphere calibration. (a) Relative luminosity profiles across the aperture. (b) Spectral radiance $L_{e,\Omega,\lambda}$.

To derive the observed radiance $L_{e,\Omega}(\text{camera})$ of the integrating sphere, the spectral radiance $L_{e,\Omega,\lambda}$ must be convoluted with the filter transmission curve $T_{\text{filter}}(\lambda)$ and integrated. The band-pass filters can be approximated by their central wavelength λ_{cwl} and full width at half maximum $\Delta\lambda_{\text{FWHM}}$ (table 3).

$$\begin{aligned} L_{e,\Omega}(\text{camera}) &= \int T_{\text{filter}}(\lambda) * L_{e,\Omega,\lambda}(\lambda)\, d\lambda \\ &\approx L_{e,\Omega,\lambda}(\lambda_{\text{cwl}}) * \Delta\lambda_{\text{FWHM}} \end{aligned} \tag{4.2}$$

For further analysis of edge particle flows, a conversion to photon flux density φ_{photon} in $\frac{\text{photons}}{\text{s}\cdot\text{sr}\cdot\text{m}^2}$ is useful. This is derived by dividing the radiance by the photon energy of the filtered wavelength λ:

$$\varphi_{\text{photon}} = \frac{L_{e,\Omega}(\text{camera})}{\frac{hc}{\lambda}}. \tag{4.3}$$

The theoretically observed photon flux φ_{photon} at the sensor is compared to the digital signal flux $\dot{S}$ measured by the cameras. Images of the integrating sphere were taken at approximate later observation distance 1.5 m, with exposure times t_{exp} (e.g., figure 19(c) for AEF10A at $t_{\text{exp}} = 4$ ms). The averaged signal S within the bright spot at the image center was divided by the exposure time to obtain the signal flux $\dot{S}$, which is proportional to the impinging photon flux. Table 4 lists the sensitivity factors for each camera in operation phases OP1.2a and OP1.2b. The sensitivity changed significantly between these phases due to a modification of the aperture (see section 6).

4.5 Filter transmission characterization

The calibration outlined earlier is limited by its simplified treatment of filter transmission. A more accurate approach involves measuring the wavelength-dependent transmission function $T_{\text{filter}}(\lambda)$ and

2025 JINST 20 T04003

Table 4. Camera sensitivities.

Camera Name	Line Filter	Sensitivity $\left[10^{10}\ \frac{\frac{\text{photons}}{\text{s·sr·m}^2}}{\frac{\text{DL}}{\text{s}}}\right]$ OP1.2a	OP1.2b
AEF10A	Hα	8200 ± 1000	143 ± 0
AEF10B	Hγ	650 ± 60	220 ± 6
AEF11A	Hα	258 ± 9	149 ± 7
AEF11B	C-III	402 ± 9	462 ± 8
AEF20A	Hα	7800 ± 1000	154 ± 0
AEF20B	C-III	2900 ± 800	255 ± 6
AEF21A	Hα	204 ± 0.5	164 ± 5
AEF21B	Hγ	381 ± 14	194 ± 7
AEF30A	Hα	146 ± 0	150 ± 0
AEF31A	Hα	122 ± 5	132 ± 2
AEF31B	Hα	212 ± 7	142 ± 4
AEF40A	Hα	212 ± 0.5	145 ± 3
AEF40B	C-II	7.5 ± 0.3	4.15 ± 0.2
AEF41A	Hα	4000 ± 1800	167 ± 7
AEF41B	C-II	6.1 ± 0.1	3.18 ± 0.1
AEF51A	Hα	570 ± 50	148 ± 43

Note: camera sensitivities for the different cameras identified by their port and position. The observed CWL of the camera is listed under "Line filter." The sensitivity is based on filter properties CWL and FWHM. The change between OP1.2a and OP1.2b is due to the adjustment from an adjustable iris to a fixed aperture, as elaborated in section 6.

integrating $T_{\text{filter}}(\lambda) \cdot L_{e,\Omega,\lambda}(\lambda)$. However, $T_{\text{filter}}(\lambda)$ depends on the angle of incidence (AOI), θ. Since the filter is situated between the lens and sensor, light rays intersect the filter at various oblique angles, not normal incidence, as illustrated in figure 21. Oblique incidence causes a blue shift of the central wavelength (CWL) [36], described by:

$$\lambda_{\text{CWL}}(\theta) = \lambda_{\text{CWL},0} \cdot \sqrt{1 - \frac{\sin^2(\theta)}{n_{\text{eff}}^2}}. \tag{4.4}$$

Assuming rotational symmetry around the optical axis, each image point at a radial distance r_{i} on the sensor receives light rays with varying AOIs. The AOI $\theta(r_{\text{i}}, r_{\text{exit}})$ is determined by the radial origin r_{exit} at the exit pupil, located at a distance d from the sensor:

$$\theta(r_{\text{i}}, r_{\text{exit}}) = \arctan \frac{r_{\text{i}} - r_{\text{exit}}}{d}. \tag{4.5}$$

Figure 22 depicts the CWL distribution for light rays originating at various radial positions r_{exit} and focusing on selected image pixels. Central pixels ($r_{\text{i}} = 0$) exhibit a narrow distribution, with minor blue shifts ($\Delta\lambda \approx 16\,\text{nm}$). In contrast, edge pixels ($r_{\text{i}} = 4\,\text{mm}$) experience larger shifts ($\Delta\lambda \approx 47\,\text{nm}$), increasing the likelihood of nuisance light contamination. Additionally, oblique incidence broadens the transmission curve, further influencing signal quality. The degree of blue shift and broadening depends on filter-specific parameters ($\lambda_{\text{CWL},0}$, n_{eff}, and $\Delta\lambda_{\text{FWHM}}$) and manufacturing variations.

2025 JINST 20 T04003

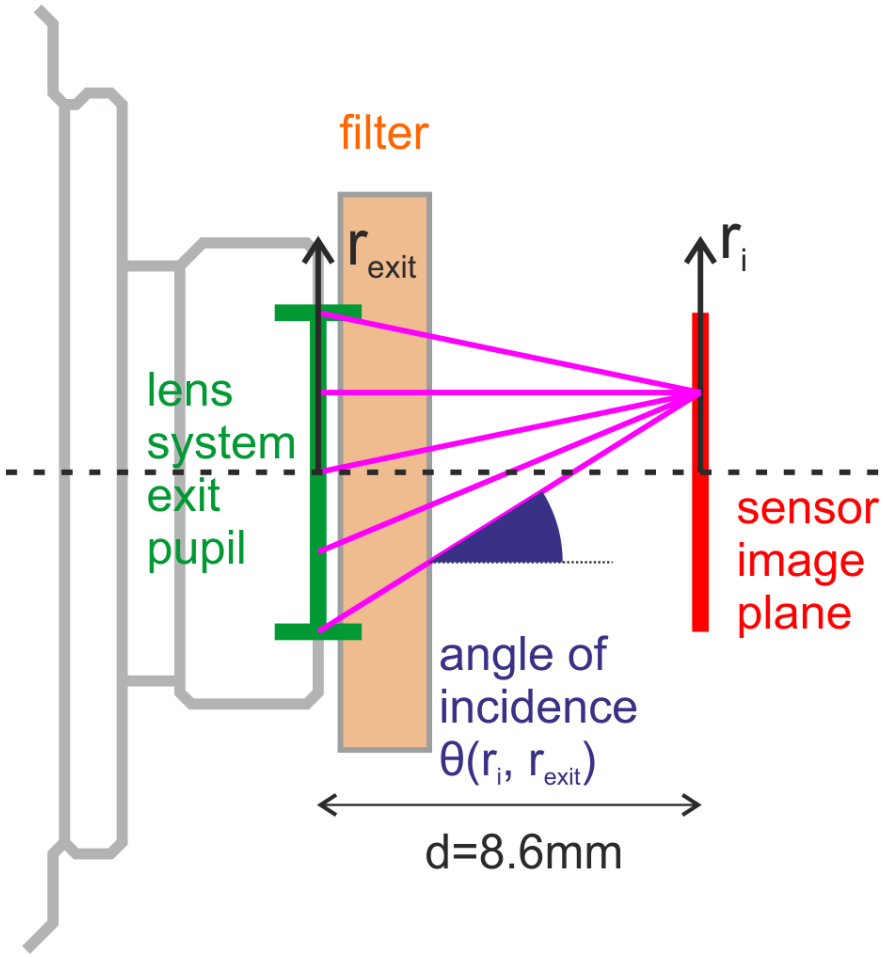

Figure 21. AOI variations. Light rays (purple) focused by the lens onto the sensor (red) pass through filter (orange) at different angles of incidence $\theta(r_{\text{exit}}, r_{\text{i}})$.

To characterize these effects, filter transmission curves were calibrated using a PerkinElmer UV/VIS/NIR Lambda 900 photometer. The experimental setup (figure 23) involved mounting the filter in a rotatable holder to allow precise angular positioning relative to the light path (accuracy $\approx 0.17°$). A monochromator scanned wavelengths in 0.1 nm steps, and the transmitted light was detected by a photomultiplier with a 0.5 s integration time. Each measurement included:

1. A dark reference to correct for sensor offsets.

2. A 100% reference using an empty filter holder.

3. Transmission measurements of the filter sample.

Fine angular scans ($\Delta\theta = 0.5°$) identified the AOI corresponding to the longest wavelength (λ_{CWL}) — a systematic offset due to filter mounting. For example, H_α filter 1 exhibited $\lambda_{\text{CWL},0} = 656.15$ nm, $\Delta\lambda_{\text{FWHM},0} = 1.6$ nm, and a peak transmissivity of $T_{\text{peak},0} = 94.7\%$ at $\theta \approx -0.5°$ (figure 24). Filters for H_γ and carbon lines were similarly calibrated.

2025 JINST 20 T04003

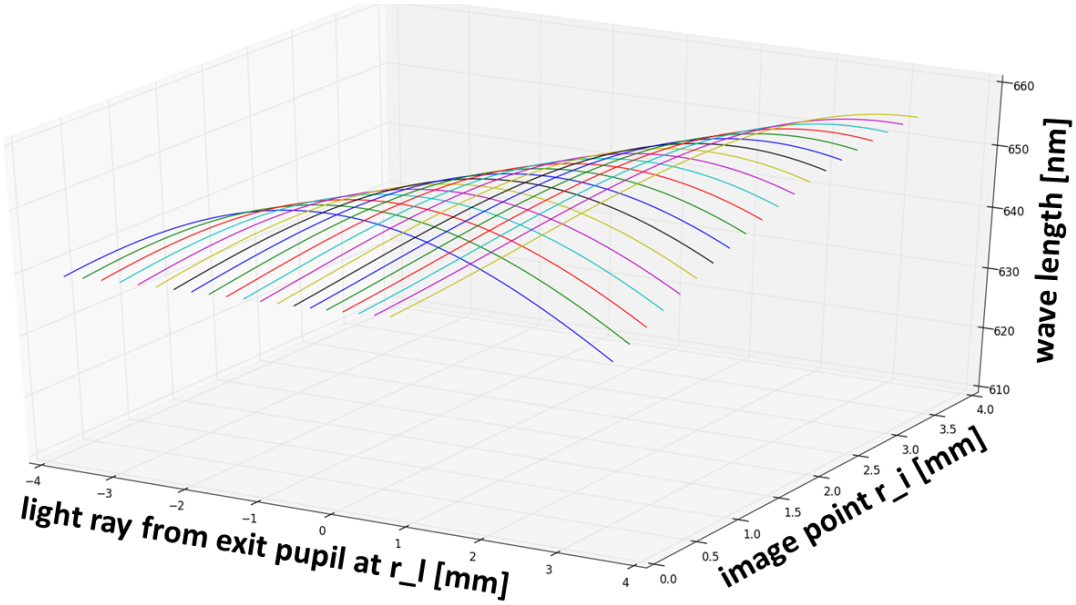

Figure 22. AOI distribution. Distribution of CWL in light rays focusing on a choice of pixels at radial position r_i on the sensor over the radial origin $r_\mathrm{l} = r_\mathrm{exit}$ at the lens.

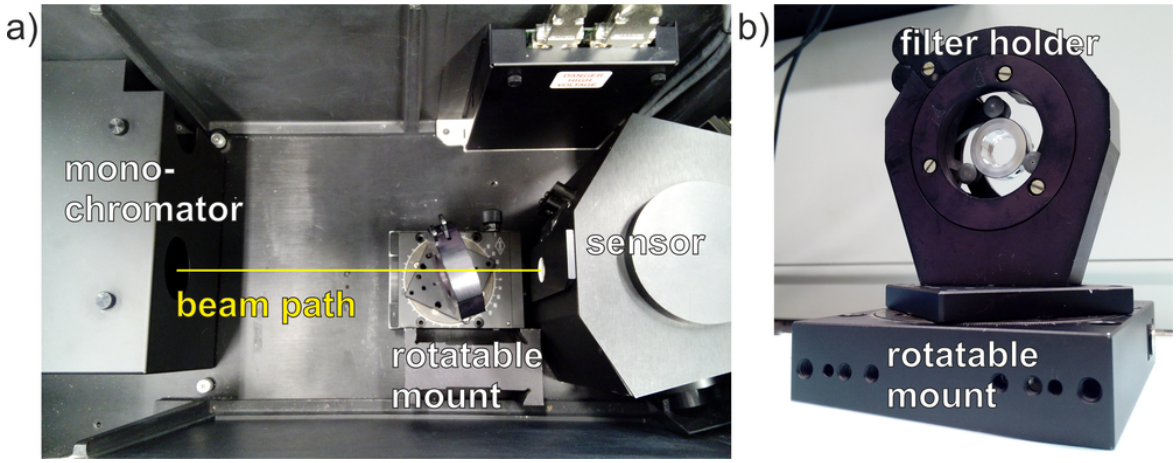

Figure 23. Setup of the filter curve calibration. (a) View inside the Perkin ELMER UV/VIS/NIR Lambda 900 photometer and (b) the rotatable mount to hold the filter.

A broader angular scan ($\Delta\theta = 5°$) revealed the AOI-dependent variation in filter parameters (figure 25). The CWL shift follows eq. 4.4, while the broadening of $\Delta\lambda_\mathrm{FWHM}$ with θ is modeled as:

$$\Delta\lambda_\mathrm{FWHM}(\theta) = \Delta\lambda_\mathrm{FWHM,0} + \Delta\lambda_\mathrm{b} \cdot \tan^2(\theta). \tag{4.6}$$

Despite some variations, peak transmissivity (T_peak) remains approximately constant and is treated as such in subsequent analyses. Figure 26 shows the normal incidence transmission curves of all H_α filters, with derived parameters summarized in table 5.

This calibration enables precise quantification of nuisance light contributions for any pixel, considering both CWL shifts and transmission curve broadening.

2025 JINST 20 T04003

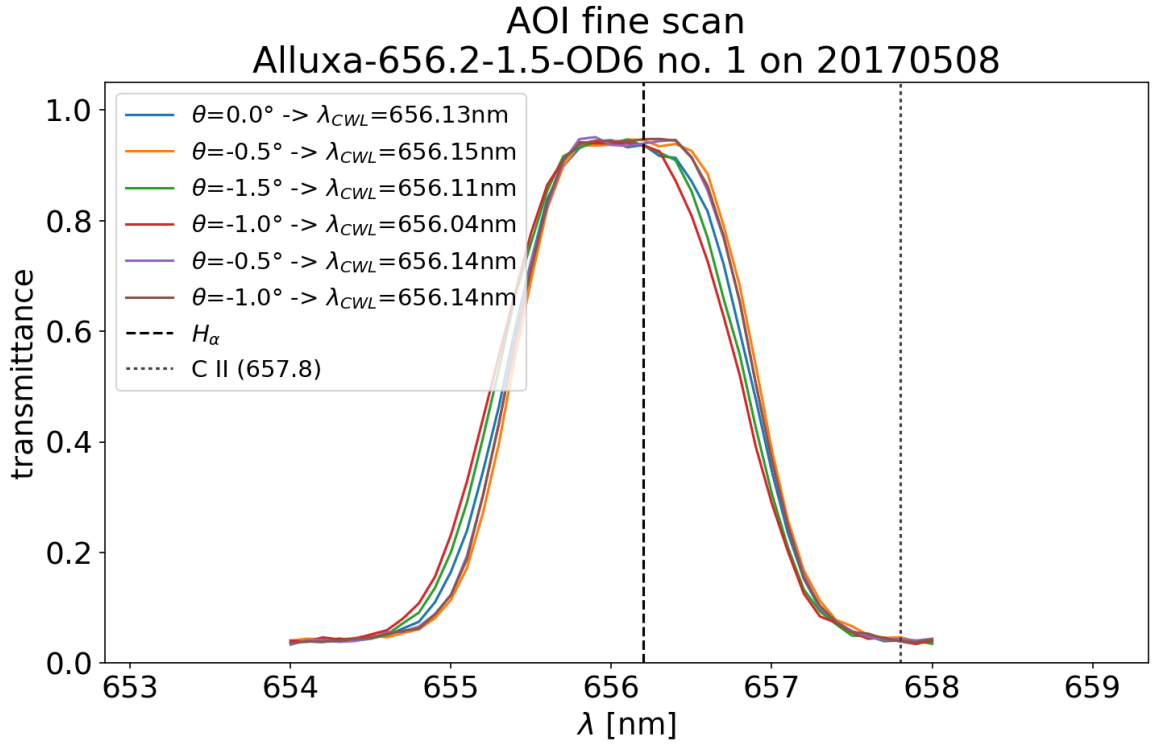

Figure 24. Filter CWL scan. An angular fine scan of the H_α filter no. 1 reveals the transmission curve for normal incidence ($\theta_0 = -0.5°$) as the one shifted furthest to longer wavelengths.

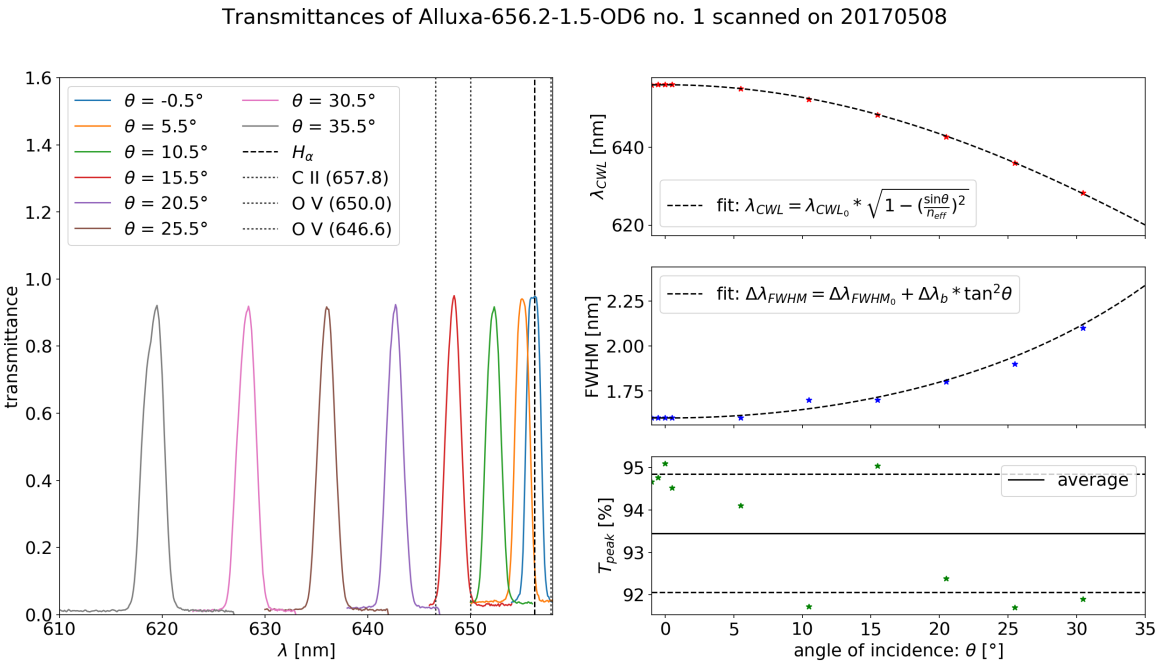

Figure 25. AOI filter scan Angular scan of the H_α filter no. 1 shows extend of shift in λ_{CWL} with AOI.

2025 JINST 20 T04003

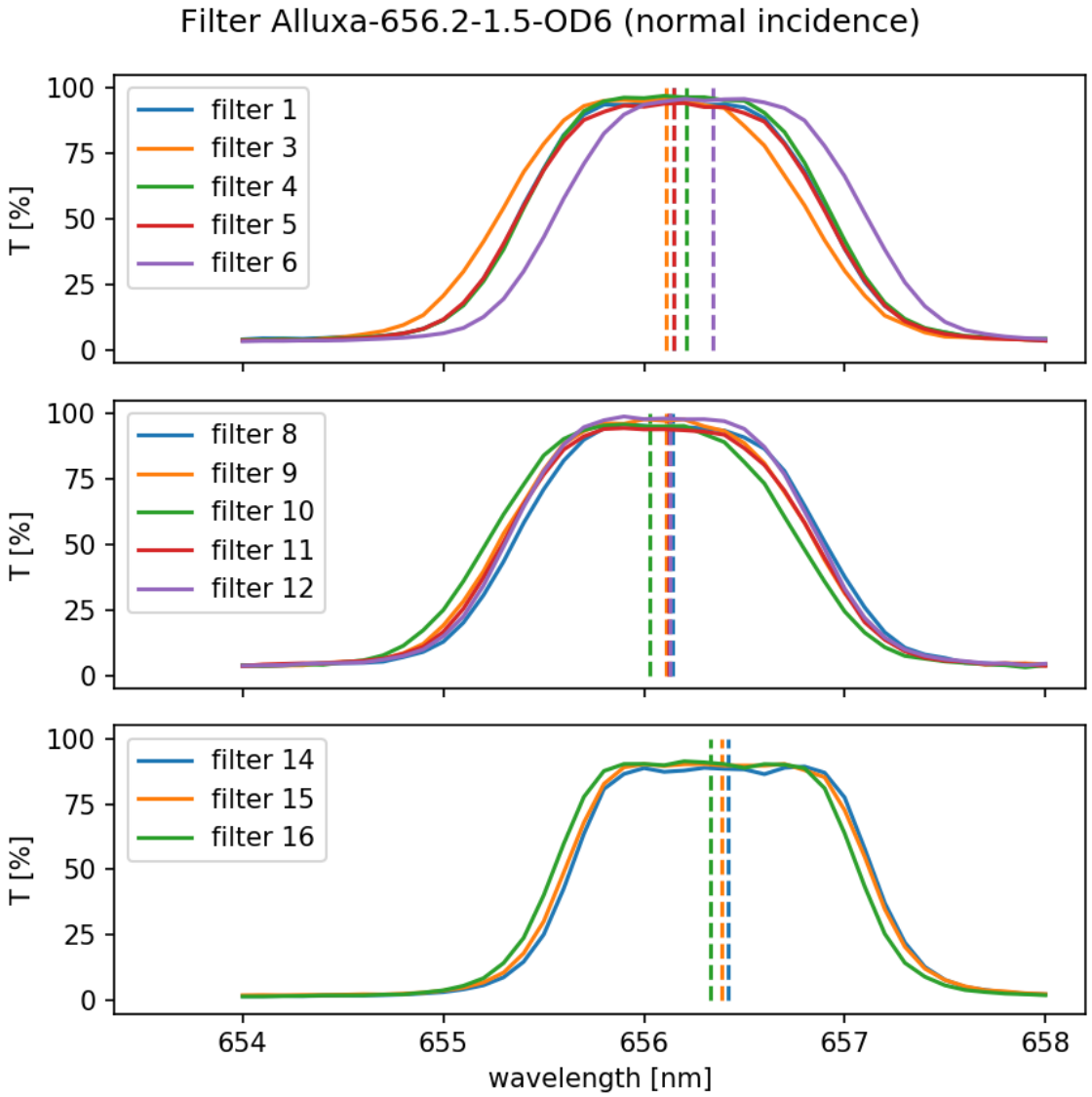

Figure 26. Normal incidence transmission. Filter transmission curves of all H_α filters at normal incidence.

4.6 Image distortion

To derive an intrinsic camera model, images of an illuminated chessboard pattern are captured across the entire FOV. This method allows for the identification of spatial distortions in the camera's imaging system. By analyzing the deformation of the regular checkerboard pattern in the recorded images, a spatial distortion model is constructed.

Images are acquired with the checkerboard placed at different positions and orientations throughout the FOV to ensure comprehensive coverage. The resulting data is used to calculate distortion parameters, which are critical for correcting geometric inaccuracies in the camera output. This camera model provides a foundation for accurate spatial calibration.

2025 JINST 20 T04003

Table 5. Filter transmission properties.

filter and no.	$\lambda_{\mathrm{CWL},0}$ [nm]	$\Delta\lambda_{\mathrm{FWHM},0}$ [nm]	$T_{\mathrm{peak},0}$ [%]	n_{eff} []	$\Delta\lambda_{\mathrm{b}}$ [nm]	$T_{\mathrm{peak,av}}$ [%]
H_α 1	656.15	1.6	94.7	1.754 ± 0.004	1.51 ± 0.05	93.5 ± 1.4
H_α 3	656.11	1.6	95.9	1.789 ± 0.002	1.39 ± 0.09	95.2 ± 1.2
H_α 4	656.21	1.6	97.0	1.782 ± 0.009	1.33 ± 0.03	96.9 ± 1.0
H_α 5	656.15	1.6	94.3	1.8012 ± 0.0017	1.23 ± 0.09	93.8 ± 1.0
H_α 6	656.34	1.6	95.9	1.777 ± 0.004	1.45 ± 0.04	94.1 ± 1.1
H_α 8	656.14	1.6	95.9	1.804 ± 0.003	1.28 ± 0.09	95.8 ± 1.2
H_α 9	656.11	1.6	97.7	1.806 ± 0.002	1.36 ± 0.09	97.0 ± 0.8
H_α 10	656.03	1.6	95.7	1.845 ± 0.009	1.20 ± 0.009	97.3 ± 1.5
H_α 11	656.12	1.6	94.4	1.769 ± 0.005	1.39 ± 0.10	94.9 ± 1.3
H_α 12	656.13	1.6	98.8	1.804 ± 0.006	1.39 ± 0.03	98.3 ± 0.8
H_α 14	656.42	1.6	99.3	1.818 ± 0.006	1.44 ± 0.05	89 ± 5
H_α 15	656.39	1.5	90.3	1.822 ± 0.008	1.8 ± 0.2	89 ± 6
H_α 16	656.33	1.6	91.4	1.827 ± 0.003	1.46 ± 0.05	90 ± 4
H_α 100	655	6	93.3	1.727 ± 0.006	3.00 ± 0.08	80 ± 30
H_γ 1	434.1	2.1	95.5	1.975 ± 0.004	0.82 ± 0.03	94.6 ± 1.3
H_γ 2	433.5	2.1	92.6	1.984 ± 0.007	0.84 ± 0.07	93 ± 3
H_γ 3	434.1	2.0	95.3	1.964 ± 0.005	1.01 ± 0.07	95 ± 2
C II 1	514.8	1.8	92.6	2.146 ± 0.006	1.46 ± 0.05	94 ± 3
C II 2	514.8	1.8	99.8	2.181 ± 0.006	1.41 ± 0.03	98 ± 2
C II 3	514.5	1.8	99.7	2.177 ± 0.007	1.36 ± 0.03	99.1 ± 1.2
C III 2	464.9	1.9	94.5	1.910 ± 0.002	1, 12 ± 0.05	93 ± 4
C III 3	464.8	1.9	96.0	1.938 ± 0.004	1.09 ± 0.07	93 ± 3
C III 7	464.6	1.9	94.1	1.938 ± 0.005	1.08 ± 0.05	93 ± 2

Note: filter transmission curve properties at normal incidence and variation parameters with AOI. The filters are indentified by the observed line and individual number. $\lambda_{\mathrm{CWL},0}$ gives the measured center wave length at normal incidence, $\Delta\lambda_{\mathrm{FWHM},0}$ the full width half maximum at normal incidence, and $T_{\mathrm{peak},0}$ the peak transmission at normal incidence angle. n_{eff} is the effective refractive index and $\Delta\lambda_b$ the spectral band offset. $T_{\mathrm{peak},av}$ gives the average peak transmission.

4.7 Extrinsic alignment to the W7-X coordinate system

The spatial calibration establishes a connection between camera images and the observed in-vessel PFC. Pixels of reference points in the divertor and baffle region are connected with the 3D W7-X coordinate system. The outcome is a set of image-like arrays that store per-pixel information about the in-vessel components intersected by each LOS. The content and usage of these array sets may vary slightly depending on the specific camera system.

General Scene Model Content:

- *x/y/z-coordinate:* LOS endpoint in the W7-X coordinate system.
- *ϕ-coordinate (toroidal):* LOS endpoint in the W7-X coordinate system.
- *θ-coordinate (poloidal):* LOS endpoint in the W7-X coordinate system.

2025 JINST 20 T04003

- *Identification number of plasma-facing component (PFC):* unique ID for the intersected PFC.
- *Angle:* between LOS and the PFC surface.
- *Distance:* between the camera and the LOS endpoint.
- *Solid angle (Ω):* observed by each pixel.
- *Surface area:* observed by each pixel, perpendicular to the LOS.

Using the surface area, the calibrated photon flux density, measured in photons/(m^2 sr s), can be converted into a photon rate in photons/(sr s) per pixel. Assuming the emission originates from the surface of a PFC, integrals over all pixels associated with a specific PFC identifier yield the total photon emission by neutrals or ions of a given plasma species at the edge. This information can be translated into the total PFC dependent neutral particle flux of that species.

4.8 Quantification of erosion and deposition on windows

The absolute calibration of the AEF51 camera system is used to assess whether surface window coatings from OP2.1 plasma operation affected transmission properties. This evaluation focuses on the H_α wavelength at 656.3 nm.

The pre-OP2.1 absolute calibration was performed on July 29, 2022, in a laboratory setup using the immersion tube with the 3D-printed front plate. The post-OP2.1 calibration, conducted on August 24, 2023, was performed in-vessel using the same immersion tube. The calibration comparison was made by analyzing the average digital level (DL) from five images for both pre- and post-OP2.1 calibrations, taken at exposure times ranging from 0.5 ms to 7 ms. Background levels, which remained consistent (DL = 300–330), were excluded from the comparison.

The post-OP2.1 absolute calibration at AEF51 in the H_α wavelength agrees within random uncertainty with the pre-OP2.1 absolute calibration, as shown in table 6. Assuming toroidal stellarator symmetry applies to the erosion/deposition behavior and that transmission changes within the observed visible range are consistent across the wavelength spectrum, no significant transmission change was detected in the immersion tube windows during OP2.1 plasma operation. Consequently, the absolute calibration for all visible cameras remained unaffected.

4.9 Inter-diagnostic comparison

To verify the quantitative accuracy of the diagnostics, measurements from the camera system were compared with those from the absolutely calibrated filterscopes [16] and divertor spectroscopy [27]. This in-situ comparison validates the calibration quality and data consistency across diagnostics, ensuring comparability.

Three filterscope channels observe H_α emission along LOS terminating on PFCs within the cameras' FOV. The LOS of both systems traverse the H_α emission zone above the observed PFCs, and emission at the PFC surface can be assumed comparable. However, this assumption breaks down for emission zones near the viewport due to distinct LOS geometries. Filterscopes, mounted in AEK ports at the outer midplane, traverse emission regions different from those observed by the cameras. As discussed in section 5, this difference can be significant, particularly for unloaded PFCs, such

2025 JINST 20 T04003

Table 6. Pre- and post-OP2.1 absolute calibration.

T_{int} [ms]	Pre OP2.1 [DL]	Post OP2.1 [DL]	Post/Pre OP2.1
0.5	581	570	98.1% ± 5.2%
1	830	830	100.0% ± 3.6%
2	1372	1328	96.8% ± 2.2%
3	1863	1839	98.7% ± 1.6%
4	2380	2345	98.5% ± 1.3%
5	2864	2836	99.0% ± 1.0%
6	3345	3333	99.6% ± 0.9%
7	3870	3844	99.3% ± 0.8%

Note: random uncertainty is based on a noise level of ±15 DL. Systematic uncertainty due to vignetting depends on the position of the integrating sphere on the image and is estimated at 3 %. Each data point represents the average of five images.

as those selected for this study. These differing LOS introduce systematic uncertainties, leading to discrepancies of up to a factor of five between measurements.

In half-module 41, the filterscope channel observes a low-loaded section of the vertical target, with a measured flux density of $1.9 \times 10^{20}\,\mathrm{m^{-2}\,s^{-1}}$, 3.5 times higher than the cameras' measurement. This discrepancy reduces to a factor of 1.8 when a control coil current of 2 kA is applied, altering the edge island topology. In half-module 51, the filterscope observes the baffle near the vertical target, recording a flux density of $2.6 \times 10^{19}\,\mathrm{m^{-2}\,s^{-1}}$, while in half-module 11, it observes the heat shield with a flux density of $3.2 \times 10^{18}\,\mathrm{m^{-2}\,s^{-1}}$. In both cases, the cameras measure flux densities lower by a factor of 0.4. Despite these discrepancies, the diagnostics agree within the expected systematic uncertainties arising from their differing LOS.

A divertor spectroscopy system, with LOS identical to the cameras, is installed in the same immersion tube at AEF51. The profile location of the divertor spectroscopy is marked by a white arrow in a camera image in figure 27. However, direct comparison with divertor spectroscopy data was challenging due to the diagnostic setup. While the H_α line is observed, its saturation in spectrometers optimized for weaker lines made H_γ a more practical comparison. H_γ measurements from AEF51 spectroscopy were compared with camera measurements from AEF21 (figure 28. The camera system consistently measured fluxes approximately 44% lower than the spectroscopy system. Additionally, a 2.5 times stronger H_α emission was observed in AEF51 compared to the AEF21 divertor unit. Accounting for these absolute H_α differences and assuming the same relationship for H_γ, the camera and spectroscopy measurements agreed within the spectroscopy's uncertainty range of 20–200%. The first maxima on the horizontal target and the minima were consistent across diagnostics. However, the maxima of the strike line on the vertical target showed an 80% higher value in the spectroscopy measurement compared to the cameras, which is explained by asymetry between divertor units.

Comparisons between the visible cameras, filterscopes, and spectroscopy diagnostics revealed systematic differences attributed to toroidal asymmetry and varying LOS. Nevertheless, within the given uncertainties, all diagnostics showed consistent agreement.

2025 JINST 20 T04003

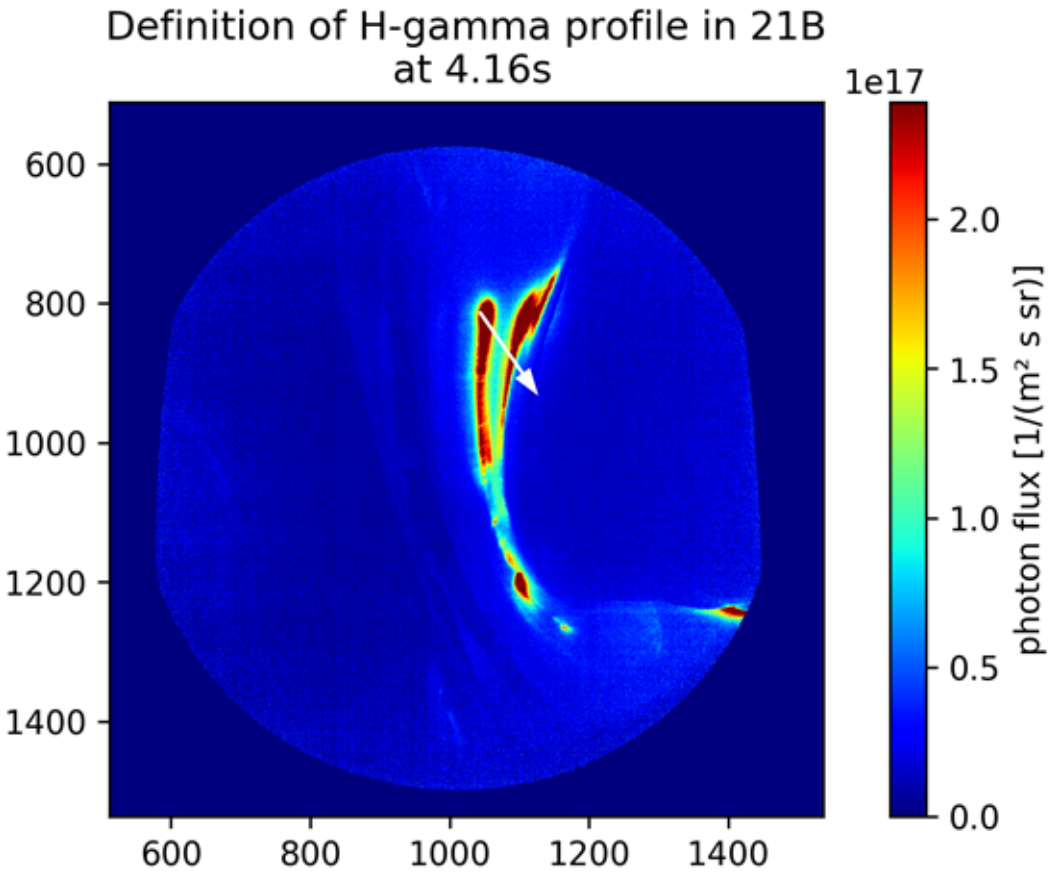

Figure 27. Profile definition for interdiagnostic comparison. H_γ image from camera 21B at 4.16 s in program ID 20181010.08. The white arrow marks the profile definition, corresponding to the observation path of the divertor spectroscopy channels in AEF51.

5 Synthetic diagnostics

The interpretation of filtered H_α camera images can be challenging, particularly when the plasma loading on a given component varies. To assist in the interpretation, synthetic diagnostics, such as those generated by EMC3-Eirene [17, 37], can provide valuable qualitative insights. One key assumption in interpreting H_α measurements is that the line emission viewed by the camera is localized to the surface being observed. While this assumption holds for regions with significant plasma load, such as the plasma strike line, it may not be valid for components with minimal plasma load, such as the baffles and inner wall heat shield.

To investigate this, a synthetic H_α camera image was generated using the synthetic diagnostic module of EMC3-Eirene [18]. The model includes both molecular and atomic contributions to the emission, with rate coefficients sourced from the AMJUEL database [38]. Figure 29(a) shows an example of an H_α image under low-density, low-radiated power conditions. The emission contributions along selected lines of sight, as labeled in figure 29(a), are shown in figures 29(b)–(f).

Several key insights can be drawn from these results. First, the emission above the plasma strike line can generally be considered a measure of the recycling flux from neutralized particles originating

2025 JINST 20 T04003

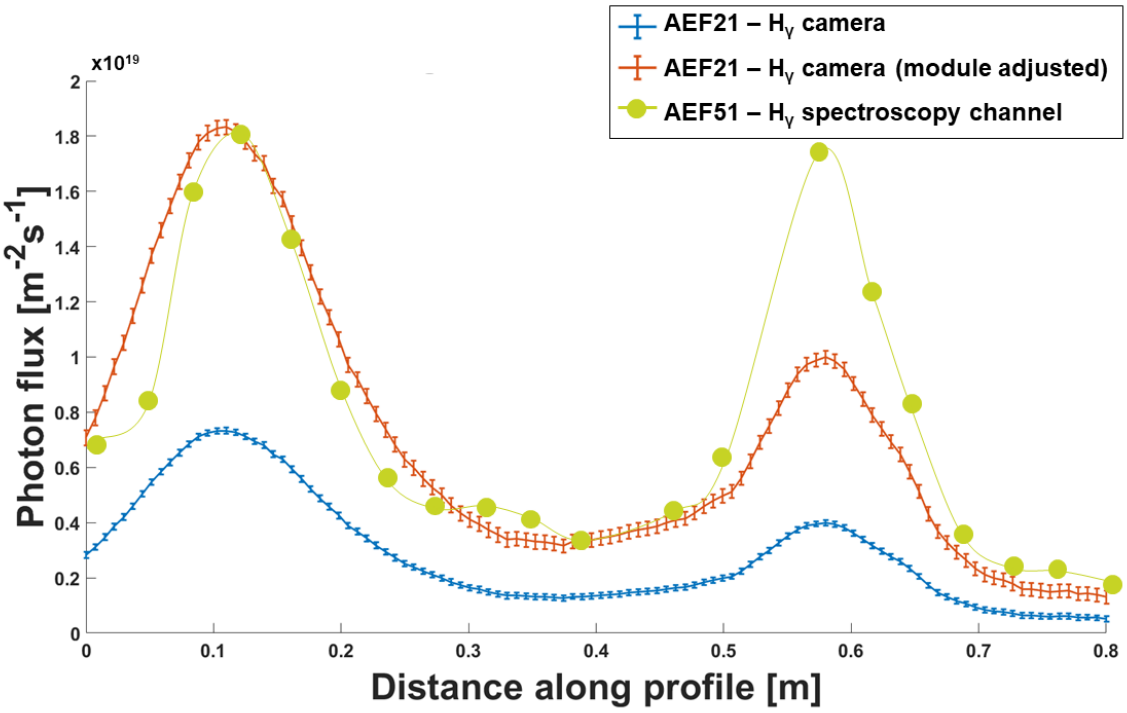

Figure 28. Interdiagnostic profile comparison. H_γ photon flux profiles from cameras and divertor spectroscopy. The original H_γ profile from AEF21 (blue) is adjusted using the H_α difference between AEF51 and AEF21 (red) and compared to the spectroscopy data from AEF51 (green).

from that surface. However, the emission from lines of sight terminating on unloaded surfaces, such as the heat shield and baffles, presents a more complex scenario. In these regions, the emission is not localized and includes significant contributions from areas both near the observed PFCs and in front of the camera. As a result, the emission cannot be directly interpreted as originating from ionization of particles locally interacting with the surface. Instead, it reflects the ionization of neutrals that have been transported from other regions of the machine, particularly the divertor strike line.

Table 7. Photon flux contribution from observed PFC side.

LOS	%	σ
Baffle, unloaded (b)	80.4522	2
Heatshield (c)	62.3318	1
Horizontal target strikeline (d)	99.8595	4
Horizontal target unloaded (e)	95.2562	3
Vertical target strikeline	99.7882	4
Baffle, loaded (f)	98.2021	3

Note: the synthetic LOS from figure 29 have been split in half and the contribution from the PFC side was quantified. LOS gives the name of the PFC on which the LOS is ending on with the subfigure from figure 29 shown in parenthesis. Note that the profile for the vertical target is not shown in the figure. % describes the likelyhood that a measured photon originates from the PFC side of the LOS. σ gives the standard deviation that a particle originates from the PFC side of the LOS.

2025 JINST 20 T04003

Quantifying the ionization flux along these lines of sight is therefore nontrivial. Since the emission is distributed along the SOL, the assumptions used in the S/XB method [39], such as localized emission with constant plasma parameters, no longer apply. Furthermore, plasma parameter measurements are typically unavailable for these unloaded regions, making direct calculation of S/XB impossible. Nevertheless, it is still possible to quantify ionization fluxes in these areas, for example, by using gas puff experiments to determine the ratio of photon flux to ionization flux [6]. Thus, while quantification of the ionization flux is more complex, these LOS can still be used to estimate the total recycling source.

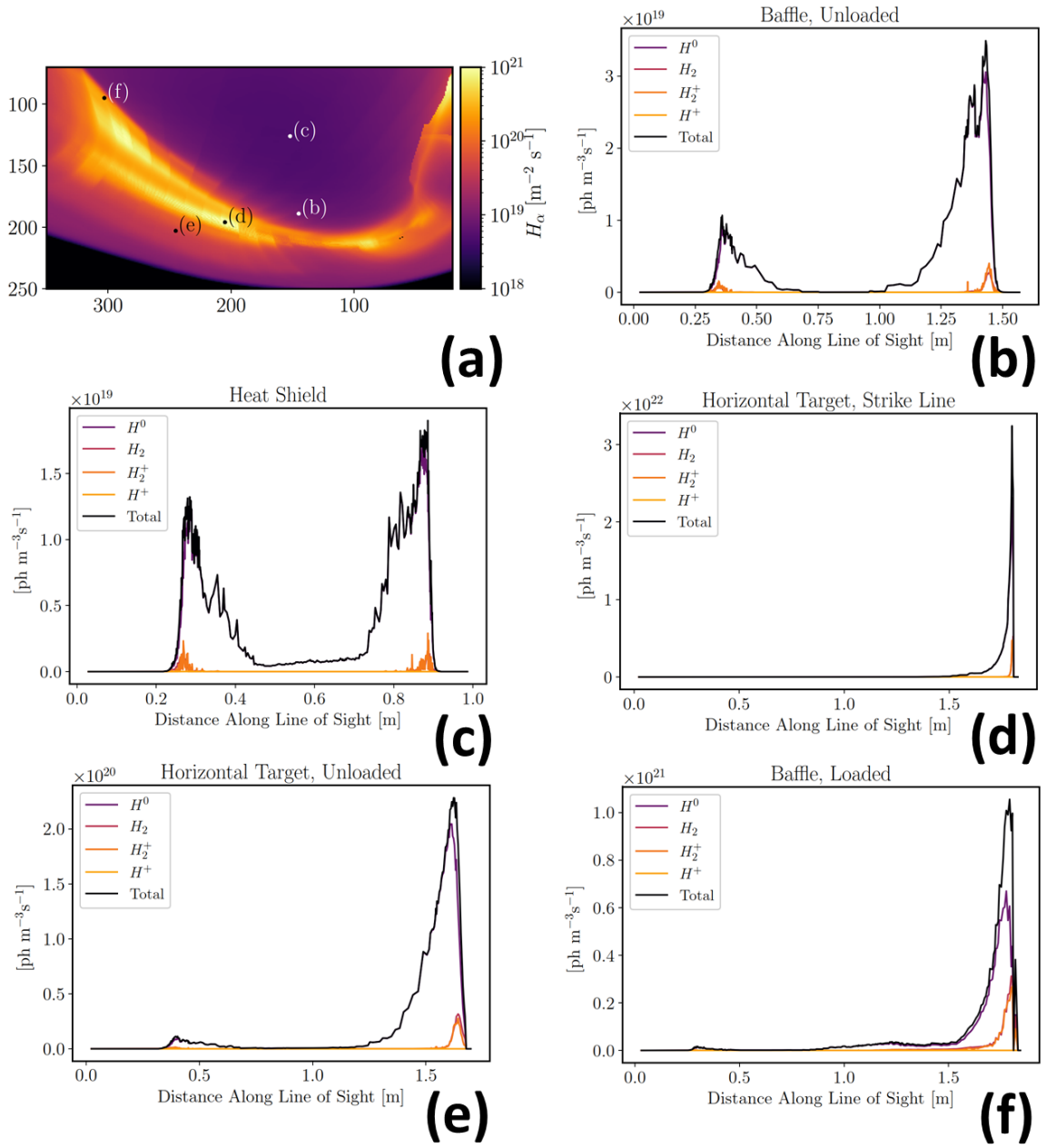

Figure 29. Synthetic diagnostic photon emission along LOS. (a) A synthetic H_α camera image. The distribution for selected pixels, labeled in (a), is plotted in (b)–(f).

6 Operational challenges

6.1 Aperture shift in OP1.2a

During OP1.2a, ferromagnetic materials in the iris aperture caused it to shift in the magnetic field, invalidating the absolute calibration of some cameras during experiments. The table 8 summarizes the time intervals during which absolute calibration remained valid for each camera. The relative uncertainty reflects variations in calibration before and after the specified intervals. For AEF30A, the pre-OP1.2a calibration was used instead of averaging pre- and post-OP1.2a calibrations, as it resulted in photon flux measurements more consistent with other well-calibrated cameras. The issue was resolved by replacing the adjustable iris with a fixed aperture in between OP1.2a and OP1.2b.

Table 8. Absolute calibration validity in OP1.2a.

Location	valid from	valid to	calibration uncertainty
AEF10A	03.11.2017	08.05.2018	12%
AEF10B	30.09.2016	08.05.2018	9%
AEF11A	14.08.2017	22.01.2018	4%
AEF11B	01.12.2016	19.01.2018	3%
AEF20A	27.10.2017	09.05.2018	14%
AEF20B	27.10.2017	09.05.2018	27%
AEF21A	14.08.2017	22.01.2018	0.4%
AEF21B	14.08.2017	22.01.2018	4%
AEF30A	15.08.2017	09.05.2018	100%
AEF31A	14.08.2017	22.01.2018	4%
AEF31B	14.08.2017	22.01.2018	3%
AEF40A	13.08.2017	09.05.2018	0.3%
AEF40B	14.11.2016	09.05.2018	4%
AEF41A	13.10.2017	09.05.2018	45%
AEF41B	11.11.2016	09.05.2018	0.5%
AEF51A	15.08.2017	11.01.2018	9%

6.2 Erroneous overexposure of individual frames

In OP1.2, bright flashes were observed in some video frames, which did not correspond to actual changes in photon flux. These flashes were artifacts caused by overexposure. The divergence in the inter-frame time before an overexposed frame was detected served as an indicator for identifying these frames. A script was developed to automatically detect and exclude overexposed frames based on this indicator, making the data usable. However, this process could not recover the lost frames.

To better understand and analyze the issue, a laboratory replica of the W7-X DAQ system was set up. Tests were conducted under varying magnetic fields, trigger settings, frame rates, and integration times. Exposure to different magnetic field vectors did not recreate the overexposure problem. The camera's frame trigger can be set to either an internal rising flank TTL or falling flank TTL trigger. During W7-X operation, the cameras are externally triggered to ensure synchronization between different systems.

2025 JINST 20 T04003

By default, the Raptor Cygnet cameras are set to trigger frames on the falling flank of a TTL pulse. A firmware setting allows the camera to be configured for a rising flank trigger. However, an error in the setup caused the camera to capture frames on both the rising and falling flanks when the rising flank trigger was selected. If a trigger occurred during the integration time of a frame, it would be ignored. However, if the integration time was shorter than the TTL pulse duration, the falling flank would trigger a new frame with a false, longer integration time, resulting in an overexposed frame.

To prevent this issue, cameras must be triggered on the falling flank of the TTL pulse. Additionally, the trigger output should be recorded to monitor the frame length and timing.

6.3 No visible DAQ software in OP2.1

Due to resource limitations and prioritization of the IR system, the development of the DAQ software for the visible camera network could not be completed by the end of OP2.1. A fallback to the previous hardware and software setup was not possible, as the old hardware had been removed to accommodate the new system. Consequently, no visible data was recorded during OP2.1.

6.4 Integration time and frame rate issues in OP2.2

During commissioning for OP2.2, issues were observed with the integration time and frame rate, both of which were found to correlate with the trigger settings.

When the magnetic field was off, integration times could be set successfully. However, with the magnetic field active, integration times could only be set using an internal trigger and not with an external trigger. Furthermore, when operating with an external trigger, the frame rate was incorrectly set to 28.5 Hz instead of the intended 25 Hz. This issue was found to be associated with the external trigger but not directly with the magnetic field.

As a workaround, all cameras have been operated with an internal trigger starting from 09.12.2024 for the remainder of OP2.2. Frames of different cameras are no longer taken synchronously, but with a time deviation of up to 20 ms. This workaround is also being considered for the next operational phase, OP2.3, which is planned to be the final phase for this system.

7 Summary

This paper presents the installation and operation of a spectroscopic camera network at Wendelstein 7-X, designed to provide spatially resolved photon flux measurements across a wide range of plasma-facing components. The system, with cameras arranged in a stellarator-symmetric configuration, achieves comprehensive coverage of 56 % of the plasma-facing surfaces, fulfilling the requirement for detailed observation of the divertor, baffles, and heat shield. The cameras operate at a frame rate of 25 Hz with spatial resolution of 1.2 to 1.4 pixel/cm.

A comparison with filterscope and divertor spectroscopy data demonstrated agreement within expected uncertainties, although discrepancies were noted in low plasma load areas, such as the heat shield and baffles, due to differing lines of sight and toroidal asymmetry. The paper also addresses an issue of overexposure in individual frames during OP1.2, caused by incorrect camera trigger settings. Laboratory tests confirmed that overexposure occurred when the integration time was shorter than the TTL pulse duration. A solution was implemented to trigger the cameras on the falling flank of the TTL pulse and monitor the trigger output to prevent this error.

2025 JINST 20 T04003

Finally, synthetic diagnostics using the EMC3-Eirene code provided insights into the emission contributions from components with minimal plasma load, emphasizing the non-localized nature of the emission. These models are critical for accurate interpretation of ionization fluxes in regions of low plasma loading. The system's comprehensive design and performance ensure reliable diagnostic data, demonstrating the importance of careful calibration and error mitigation in fusion diagnostics.

8 Outlook

The system described in this publication is planned to be decommissioned following OP2.3, which is scheduled to occur from March to May 2025. For OP2.4, the immersion tubes will be replaced with a newly developed endoscope system [24]. This upgraded system offers significant improvements, including a 4.5-fold enhancement in spatial resolution, a 4-fold increase in maximum temporal resolution, and higher light sensitivity. The new FOV will encompass the entire divertor targets and surrounding baffles but will exclude PFCs outside this region.

First images from the endoscope system were captured in March 2023, demonstrating a spatial resolution of 6.4 pixels/cm at frame rates of up to 100 Hz. The spatial resolution was determined by measuring a prominent gap in the baffle from the camera image (figure 30(a)) and comparing it to the corresponding feature in a CATIA model (figure 30(b)).

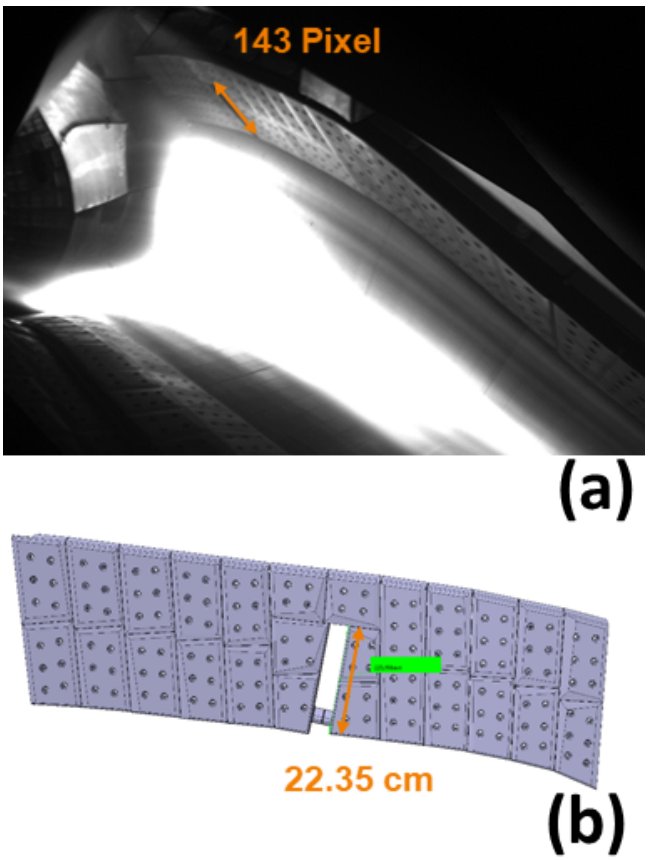

Figure 30. Endoscope spatial resolution. Two images illustrating the determination of the endoscope system's spatial resolution. (a) Overexposed camera image highlighting the baffle structure, with the gap measured at 143 pixels. (b) CATIA model of the baffle section, where the corresponding gap measures 22.35 cm in length.

2025 JINST 20 T04003

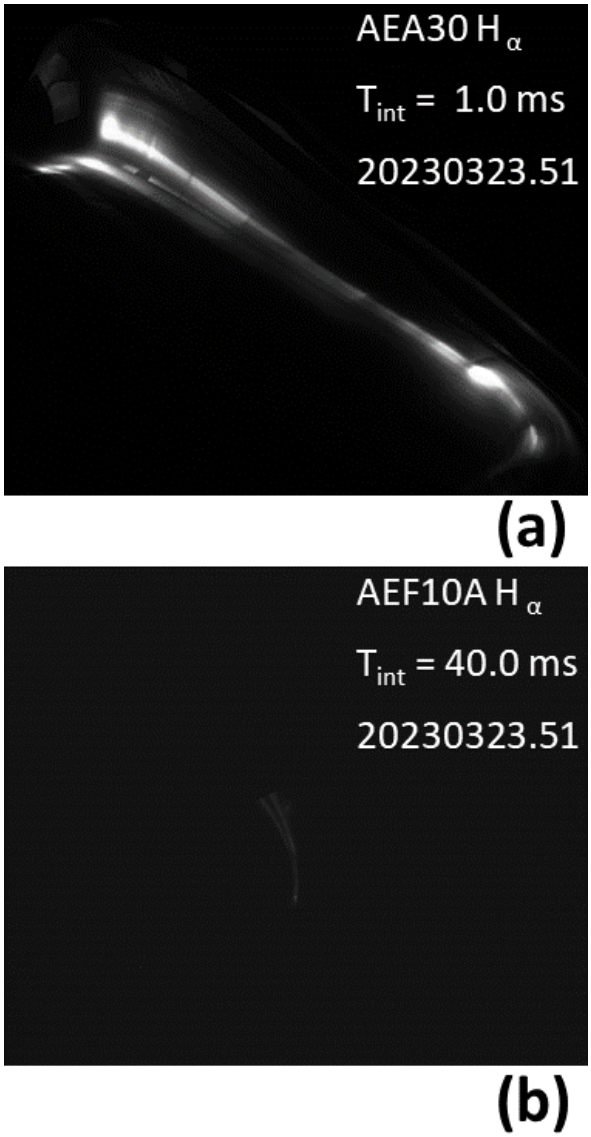

Figure 31. Comparison of endoscope and immersion tube systems. Images from the same program ID (20230323.51) and time, highlighting differences in light sensitivity. (a) Endoscope image captured with an integration time of 1.0 ms, appearing significantly brighter. (b) Immersion tube image captured with an integration time of 40.0 ms, demonstrating lower light sensitivity.

Although the increase in light sensitivity has not been quantitatively determined, qualitative comparisons revealed a substantially brighter strike line in the endoscope image at just 1/40th of the integration time of an immersion tube image.

Acknowledgments

This work has been carried out within the framework of the EUROfusion Consortium, funded by the European Union via the Euratom Research and Training Programme (Grant Agreement No 101052200 — EUROfusion). Views and opinions expressed are however those of the author(s) only and do not

2025 JINST 20 T04003

necessarily reflect those of the European Union or the European Commission. Neither the European Union nor the European Commission can be held responsible for them.

We acknowledge the use of code "QSR" for data calibration, post-processing and analysis, available at https://gitlab.mpcdf.mpg.de/pdd/QSR, Commit: 7c4966be67c7e31bcc6f733e4516131c8ac5c769.

We would like to acknowledge the assistance of ChatGPT, an AI language model developed by OpenAI, for its valuable support in refining the language of this paper.

References

[1] O. Grulke et al., *Overview of the first Wendelstein 7-X long pulse campaign with fully water-cooled plasma facing components*, *Nucl. Fusion* **64** (2024) 112002.

[2] G. Grieger et al., *Physics optimization of stellarators*, *Phys. Fluids B* **4** (1992) 2081.

[3] A. Peacock et al., *Progress in the design and development of a test divertor (TDU) for the start of W7-X operation*, *Fusion Eng. Des.* **84** (2009) 1475.

[4] T. Klinger et al., *Overview of first Wendelstein 7-X high-performance operation*, *Nucl. Fusion* **59** (2019) 112004.

[5] R. König et al., *The divertor program in stellarators*, *Plasma Phys. Control. Fusion* **44** (2002) 2365.

[6] T. Kremeyer et al., *Analysis of hydrogen fueling, recycling, and confinement at Wendelstein 7-X via a single-reservoir particle balance*, *Nucl. Fusion* **62** (2022) 036023.

[7] V.R. Winters et al., *Overview of the plasma-surface interaction on limiter surfaces in the startup campaign of Wendelstein 7-X*, *Phys. Scripta* **2017** (2017) 014050.

[8] T. Barbui et al., *The He/Ne beam diagnostic for line-ratio spectroscopy in the island divertor of Wendelstein 7-X*, 2019 *JINST* **14** C07014.

[9] T. Barbui et al., *Measurements of plasma parameters in the divertor island of Wendelstein 7-X through line-ratio spectroscopy on helium*, *Nucl. Fusion* **60** (2020) 106014.

[10] O.P. Ford et al., *Charge exchange recombination spectroscopy at Wendelstein 7-X*, *Rev. Sci. Instrum.* **91** (2020) 023507.

[11] D. Gradic et al., *Impurity temperatures measured via line shape analysis in the island scrape-off-layer of Wendelstein 7-X*, *Plasma Phys. Control. Fusion* **64** (2022) 075010.

[12] E. Wang et al., *Impurity sources and fluxes in W7-X: from the plasma-facing components to the edge layer*, *Phys. Scripta* **2020** (2020) 014040.

[13] R. König et al., *The Set of Diagnostics for the First Operation Campaign of the Wendelstein 7-X Stellarator*, 2015 *JINST* **10** P10002.

[14] M. Krychowiak et al., *Overview of diagnostic performance and results for the first operation phase in Wendelstein 7-X*, *Rev. Sci. Instrum.* **87** (2016) 11D304.

[15] D. Hathiramani et al., *Upgrades of edge, divertor and scrape-off layer diagnostics of W7-X for OP1.2*, *Fusion Eng. Des.* **136** (2018) 304.

[16] R.J. Colchin et al., *The Filterscope*, *Rev. Sci. Instrum.* **74** (2003) 2068.

[17] V.R. Winters et al., *EMC3-EIRENE simulation of first wall recycling fluxes in W7-X with relation to H-alpha measurements*, *Plasma Phys. Control. Fusion* **63** (2021) 045016.

[18] H. Frerichs et al., *Synthetic plasma edge diagnostics for EMC3-EIRENE, highlighted for Wendelstein 7-X*, *Rev. Sci. Instrum.* **87** (2016) 11D441.

2025 JINST 20 T04003

[19] S. Marsen et al., *First results from protective ECRH diagnostics for Wendelstein 7-X*, *Nucl. Fusion* **57** (2017) 086014.

[20] S. Äkäslompolo et al., *Validating the ASCOT modelling of NBI fast ions in Wendelstein 7-X stellarator*, 2019 *JINST* **14** C10012.

[21] S. Äkäslompolo et al., *Armoring of the Wendelstein 7-X divertor-observation immersion-tubes based on NBI fast-ion simulations*, *Fusion Eng. Des.* **146** (2019) 862.

[22] S. Sereda et al., *Impact of boronizations on impurity sources and performance in Wendelstein 7-X*, *Nucl. Fusion* **60** (2020) 086007.

[23] M. Jakubowski et al., *Infrared imaging systems for wall protection in the W7-X stellarator*, *Rev. Sci. Instrum.* **89** (2018) 10E116.

[24] J. Fellinger, M. Schülke, M. Krause and Y. Gao, *Manufacturing, installation, commissioning and operation of endoscopes for monitoring water-cooled divertor in Wendelstein 7-X*, *Fusion Eng. Des.* **203** (2024) 114413.

[25] D. Chauvin, M. Jakubowski, H. Jenzsch et al., *Design and manufacturing progress of irvis endoscopes prototypes for W7-X divertor temperature monitoring*, in the proceedings of the *29th Symposium on Fusion Technology*, Prague, Czech Republic, September 5–9 (2016).

[26] V. Perseo et al., *Coherence imaging spectroscopy at Wendelstein 7-X for impurity flow measurements*, *Rev. Sci. Instrum.* **91** (2020) 013501.

[27] M. Krychowiak, R. König, F. Henke et al., *Gaussian process tomography of carbon radiation in the transition to detached plasmas in the Wendelstein 7-X stellarator*, in the proceedings of the *47th EPS Conference on Plasma Physics*, Sitges, Spain, June 21–25 (2021).

[28] S. Zoletnik et al., *First results of the multi-purpose real-time processing video camera system on the Wendelstein 7-X stellarator and implications for future devices*, *Rev. Sci. Instrum.* **89** (2018) 013502.

[29] H. Greuner, B. Boeswirth, J. Boscary and P. McNeely, *High heat flux facility GLADIS:. Operational characteristics and results of W7-X pre-series target tests*, *J. Nucl. Mater.* **367** (2007) 1444.

[30] A. Puig Sitjes et al., *Wendelstein 7-X Near Real-Time Image Diagnostic System for Plasma-Facing Components Protection*, *Fusion Sci. Technol.* **74** (2018) 116.

[31] D. Beiersdorf et al., *Qualification of the laser powder bed fusion (L-PBF) manufacturing process for water-cooled protective components made from 316L for plasma-exposed use in the Stellarator fusion device Wendelstein 7-X*, *Fusion Eng. Des.* **196** (2023) 114018.

[32] *My125m product description*, 2007–2019.

[33] A. Winter et al., *Preparation of W7-X CoDaC for OP2*, *IEEE Trans. Plasma Sci.* **48** (2020) 1779.

[34] H. Laqua et al., *Experiences with the Segment Control system at Wendelstein 7-X operation*, *Fusion Eng. Des.* **123** (2017) 588.

[35] C. Hennig et al., *ArchiveDB — Scientific and technical data archive for Wendelstein 7-X*, *Fusion Eng. Des.* **112** (2016) 984.

[36] P.W. Baumeister, *Optical Coating Technology*, SPIE Press, Bellingham, WA, U.S.A. (2004) [DOI:10.1117/3.548071].

[37] H. Frerichs et al., *Reconstruction of recycling flux from synthetic camera images, evaluated for the Wendelstein 7-X startup limiter*, *Nucl. Fusion* **57** (2017) 126022.

[38] P. Börner, *Additional atomic and molecular data for EIRENE*, https://www.eirene.de/old_eirene/html/amjuel.html.

2025 JINST 20 T04003

[39] S. Brezinsek et al., *Characterization of the deuterium recycling flux in front of a graphite surface in the TEXTOR tokamak*, *Plasma Phys. Control. Fusion* **47** (2005) 615.